Top-down nanostructured multilayer MoS2 with atomically sharp edges for electrochemical hydrogen evolution reaction

Materials Today Nano 25 (2024) 100467

Contents lists available at ScienceDirect

Materials Today Nano

journal homepage: www.sciencedirect.com/journal/materials-today-nano

Top-down nanostructured multilayer MoS_2 with atomically sharp edges for electrochemical hydrogen evolution reaction

Alexander Yu. Polyakov [a,b,*], Serge Al Bacha [c,d], Waleed M.A. El Rouby [c], Battulga Munkhbat [a,e], Loïc Assaud [d], Pierre Millet [c,d], Björn Wickman [a,*], Timur O. Shegai [a,*]

[a] Department of Physics, Chalmers University of Technology, Göteborg, 412 96, Sweden
[b] SMENA Catalysis AB, Göteborg, 412 96, Sweden
[c] Elogen, 8 Avenue du Parana, Les Ulis, 91940, France
[d] ICMMO-CNRS UMR 8182, Université Paris-Saclay, 17 Avenue des Sciences, Orsay, 91400, France
[e] Department of Electrical and Photonics Engineering, Technical University of Denmark, Ørsteds Plads, Kongens Lyngby, 2800, Denmark

ARTICLE INFO

Keywords:
Water splitting
Green hydrogen production
Zigzag edges
Scanning electrochemical microscopy
Nanoelectrochemistry
Single-particle electrode

ABSTRACT

Cost-efficient and readily scalable platinum-free electrocatalysts are crucial for a smooth transition to future renewable energy systems. Top-down activation of MoS_2 promises the production of sustainable hydrogen evolution electrocatalysts from the Earth-abundant molybdenite ore. Here, the deterministic nanopatterning of multilayer MoS_2 with numerous zigzag edges is explored as a pathway to enhance hydrogen evolution reaction (HER). Nanopatterned single-nanosheet MoS_2 electrodes are assessed by two highly localized electrochemical techniques: selected area voltammetry (with lithography-defined regions of electrode-electrolyte contact) and Scanning ElectroChemical Microscopy (SECM). The nanopatterning effect is the most pronounced after prolonged electrochemical cycling in an acidic electrolyte. The electrocatalytic hydrogen evolution activity of edge-enriched electrodes is dramatically enhanced: the maximum electrochemical current density (j_{max}) achieved at -510 mV *vs.* reversible hydrogen electrode (mV_{RHE}) is increased by two orders of magnitude, reaching >300 mA·cm^{-2}. Both the η_{10} and η_{100} overpotentials are significantly reduced as well. Meanwhile, pristine MoS_2 shows just ≈6 times j_{max} increase (≈30 mA·cm^{-2}) after the very same cycling. The increased electrocatalytic activity comes with electrode morphology degradation, evidenced by *ex-situ* scanning electron microscopy. SECM directly visualizes stronger HER activity in the regions with densely located zigzag edges. Intense white light illumination significantly boosts HER on MoS_2 electrodes due to the photo-enhanced MoS_2 conductivity. These results improve the understanding and reveal the limitations of MoS_2-based electrocatalytic water splitting.

1. Introduction

Hydrogen is a key component for renewable energy transition because of its high gravimetric energy density (39 kWh·kg^{-1}), clean oxidation byproducts, and broad possibilities for decarbonizing multiple industry sectors. Currently, only 4% of hydrogen is produced by fossil-free technologies, mainly water electrolysis. Alkaline water electrolysis (AWE) and proton-exchange membrane water electrolysis (PEMWE) are two prominent industrial techniques for green hydrogen production [1,2]. PEMWE offers distinct advantages over AWE, including higher efficiency and current densities, increased H_2 production per volume of the electrolyzer, faster response, and excellent compatibility with variable and partial power loads, making it suitable for integration with renewable energy sources (like wind turbines or photovoltaic cells) and decentralized hydrogen production [3]. However, strong acidic conditions in PEMWE rule out nearly all cheap transition metal catalysts, such as nickel, used in AWE. Therefore, further scaling of green hydrogen production by PEMWE is limited by the high cost and scarcity of platinum group metal (PGM) electrocatalysts.

PEMWE implies hydrogen evolution reaction (HER) on the cathode and oxygen evolution reaction (OER) on the anode. In recent decades, numerous alternative electrocatalysts for HER were developed and showed high activity on a lab scale [4]. Nowadays, nanostructured transition metal phosphides and carbides exhibit the best overpotential and Tafel slope values among candidate platinum-free electrocatalysts for hydrogen production [4–6]. Transition metal dichalcogenides (TMDs)

* Corresponding authors.
E-mail addresses: aleksandr.poliakov@chalmers.se (A.Yu. Polyakov), bjorn.wickman@chalmers.se (B. Wickman), timurs@chalmers.se (T.O. Shegai).

https://doi.org/10.1016/j.mtnano.2024.100467
Received 12 September 2023; Received in revised form 6 February 2024; Accepted 26 February 2024
Available online 1 March 2024

with metallic conductivity are highly active as well and maintain stability at current densities of >5000 mA·cm^{-2} [7]. However, most of these numerically outstanding electrocatalysts require a complex chemical synthesis and suffer from high costs and related scalability issues up to industrial amounts [6]. In turn, molybdenum disulfide (MoS_2) [8,9] is still an attractive candidate due to the potential large-scale production of efficient HER catalysts from cheap and Earth-abundant natural mineral molybdenite. Moreover, a moderate band gap (*ca.* 1.2 eV indirect transition) enables strong enhancement of MoS_2 electronic and electrocatalytic properties by visible to near-infrared solar light [10,11].

In the most thermodynamically stable and abundant 2H-MoS_2 phase, HER activity is limited to zigzag edges and other unsaturated sites such as sulfur vacancies [12] and Frenkel defects [13]. The defect-free basal plane is relatively inert [14]. As a result, several approaches have been explored to enhance the density of accessible defects in 2H-MoS_2 or achieve novel active sites with higher intrinsic activity *via* heteroatom doping, heterostructure fabrication, intercalation, phase engineering, *etc.* [15–21]. The latter strategy led to a few record-setting electrocatalysts, albeit complex and potentially hard to scale [22–26]. For instance, lithium intercalation in a battery configuration resulted in the lowered oxidation state of Mo and partial 2H → 1T phase transition, enabling as low as 200 mV HER overpotential at 200 mA·cm^{-2} [22] and the Tafel slopes down to 44 mV·dec^{-1} (ALD-synthesized edge-terminated MoS_2 + lithiation) [23]. MoS_2 nanosheets with a very high concentration of 1T phase were also prepared *via* $LiBH_4$-based chemical exfoliation in an Ar atmosphere. These nanosheets exhibited HER Tafel slope of *ca.* 40 mV·dec^{-1} and minimal performance deterioration upon partial oxidation [24]. Mesoporous 1T-MoS_2 nanosheets prepared by liquid-ammonia-assisted lithiation (LAAL) have similarly low (43 mV·dec^{-1}) Tafel slope albeit larger overpotential values [25]. Extremely low overpotential of *ca.* 43 mV @ 10 mA·cm^{-2} and Tafel slope of 34 mV·dec^{-1} was achieved by hydrothermal synthesis of phosphorus-doped MoS_2 nanosheets [26].

MoS_2 defect engineering either pursues atomic-level surface modulation to generate sulfur vacancies and other point defects [12,13,27–29] or aims at maximized exposure of edge sites and grain boundaries by manufacturing mesoporous, nanostructured, or vertically oriented MoS_2 [30–35]. However, the known techniques mostly rely on bottom-up chemical syntheses, including chemical vapor deposition (CVD) [33,36], template-guided sulfidization of Mo films [30], MoO_2 [37], MoO_3 [31], or hexaammonium heptamolybdate [35], decomposition of thiomolybdates [34], *etc*. Unfortunately, these techniques are hardly scalable towards even the hundreds-gram level (especially CVD). Furthermore, they usually require purified molybdenum-containing precursors, which significantly increase the cost of the final electrocatalysts.

Top-down techniques for MoS_2 defect engineering/enrichment are essentially more attractive from the industrial perspective because, ultimately, they may enable large-scale activation of natural MoS_2. They involve partial destruction or perforation of preliminary synthesized or natural bulk MoS_2 crystals, flakes, or powders to increase the number of HER-active sites. However, numerical HER descriptors of the top-down activated MoS_2 are typically more modest[1] than the ones of phase-engineered and heteroatom-doped MoS_2. Top-down activation is studied in more detail for CVD-grown and mechanically exfoliated MoS_2 immobilized on a substrate, while controllable activation of powders and colloids is less mature. In contrast, the industrial applicability of these techniques towards natural MoS_2 processing decreases in the following order (depending on the MoS_2 type they were developed for): commercial powders ≫ flakes exfoliated from bulk MoS_2 > bottom-up synthesized nanosheets ≈ CVD-grown multilayers > CVD-grown monolayers.

Grinding down to the smallest lateral particle size is one of the most obvious strategies to increase the gravimetric edge content in MoS_2 powders. Ionic-liquid-assisted grinding exfoliation with subsequent cascade centrifugation was used to produce few-layer MoS_2 nanodots with plenty of exposed active HER sites from commercial MoS_2 powder [38]. Prolonged ball milling and ultrasonication were used to activate hydrothermally synthesized MoS_2 nanosheets [39]. Both methods require multiple energy-consuming and limited-yield steps.

Immobilized MoS_2 can be *randomly* enriched with HER active sites by plasma treatment. Relatively mild argon [12,40,41] and hydrogen [42] plasmas can generate S-vacancies [12,42], domain boundaries, and 1T phase grains [40]. In turn, oxidative oxygen plasma [41,43,44] usually results in harsher surface damages like micro-cracks and saw-toothed edges [43,44] and the incorporation of oxygen-based Mo^{5+}, Mo^{6+}, and S^{6+} species [41]. MoS_2 nanosheet colloids can be activated with S-vacancies by illumination with a nanosecond pulsed Nd:YAG (1064 nm) laser [45]. However, these methods are not scalable.

Chemical activation methods are essentially more scalable because the interaction of the activating agent with MoS_2 can be uniformly distributed over the solid-gas or solid-liquid interface, and they do not require plasma or laser sources. High-temperature (700 – 800°C) annealing in hydrogen can activate the basal plane of CVD-grown edge-rich MoS_2 nanoplatelets by introducing irregular nanopores and nanostrips [43]. Annealing in 500 – 700°C in water steam / Ar gas mixture resulted in the activation of 1 – 5 layer and multilayer exfoliated flakes and bulk MoS_2 crystals [46]. Different etching patterns terminated with zigzag edges could be achieved depending on the annealing temperature. Sodium hypochlorite (NaOCl) was shown to be a suitable chemical to increase the edge content of MoS_2 powder, exfoliated flakes, and CVD-grown monolayer [47]. Oxygen plasma treatment was crucial to pre-activate the surface before the chemical etching. Perforated nanosheets (hence, with increased edge content) were produced from commercial MoS_2 powder *via* oxidative exfoliation using another common oxidant, H_2O_2 [48]. Note that we further compare and discuss the electrochemical performance of top-down activated MoS_2 in Fig. 4 (Chapter 3.2) and the Supporting Information (Chapter S6).

In recent years, a few techniques were developed for *deterministic* top-down activation of MoS_2. Typically, it implies the fabrication of densely and precisely arranged edge sites. Dense arrays of circular holes with random edges were drilled in monolayer MoS_2 by Ar ion beam etching through an ultrathin anodic alumina mask [49]. High-resolution patterning of polycrystalline multilayer CVD-grown MoS_2 film was also performed using a focused ion beam [50]. The periodic arrays were designed based on COMSOL simulations of electric potential distribution [50]. Recently, moderately controllable circular hole arrays were patterned in CVD-grown mono-to-trilayer MoS_2 by O_2 plasma etching through the mask prepared by block copolymer lithography. Then, the holes were converted into zigzag-edge terminated triangular nanopores by wet etching in potassium ferricyanide solution [51]. Anisotropic oxidative etching of TMDs dates to the 1960s – 1980s [52–59]. However, only in 2020, Prof. Timur Shegai's group reported a nanofabrication protocol combining deterministically nanopatterned dry-etched holes with anisotropic wet etching to produce edge-enriched multilayered TMD metamaterials [60]. The combination of electron beam lithography (EBL), CHF_3 plasma dry etching, and H_2O_2-based wet etching resulted in excellent spatial precision, atomic sharpness of zigzag edges, and high-quality etching pit walls, which were not achieved by any similar TMD nanopatterning technologies [50,51,61–64].

The stability of MoS_2 electrodes during HER is paramount for molybdenite commercialization in PEM electrolyzers. However, the data available so far is diverse and possibly dependent on the method of electrocatalyst preparation. In many reports, prolonged chronoamperometry and/or multiple voltammetry cycles led to a negligible or minor decrease in the electrochemical performance of electrocatalysts [23,26,28,29,39–45,47,50,51]. However, the morphological changes of the electrodes were not studied. In contrast, a beneficial effect of elec-

[1] Except the cases when the initial molybdenite is synthesized by hydrothermal methods.

trochemical cycling was revealed in other publications. It was shown, for instance, that the HER performance of oxidized 2H-MoS_2 was restored after 150 electrochemical cycles [24]. Cycling to negative potentials in 0.5 M H_2SO_4 also remarkably improved HER activity of MoS_2 nanosheets synthesized by ambient-pressure CVD [65]. This effect was attributed to proton intercalation, but no morphology or flake distribution changes were observed [65]. In turn, a dramatic improvement of the HER activity of H-TaS_2 and H-NbS_2 after thousands of cycles between +0.2 V and -0.6 V *vs.* reversible hydrogen electrode (V_{RHE}) was associated with a major morphological evolution: the nanoplatelets became thinner, smaller, and more dispersed, without changes in chemical composition [66]. Such "self-optimizing" changes were also explained by proton intercalation and H_2 nanobubble formation between the disulfide layers, which eventually perforates or peels them away. The electrochemical generation of S-vacancies was observed during 60 seconds of chronoamperometry of polycrystalline multilayer 2H-MoS_2 below -0.6 V_{RHE} [27]. Other publications also reported the electrochemical dissolution of MoS_2 during HER [67] or used cycling as a preliminary step before measuring reliable results [24,68]. In this context, deterministically nanopatterned single-particle electrodes can shed light on the evolution of MoS_2 morphology and HER electrocatalytic activity during prolonged electrochemical cycling.

Here, we employ our deterministic nanofabrication technique [60] to produce edge-enriched single-particle electrodes based on immobilized multilayer MoS_2 flakes. Well-defined arrays of the etching pits bordered by the atomically sharp zigzag edges enabled highly localized assessment of the activated MoS_2: selected area voltammetry corroborated with *ex-situ* scanning electron microscopy (SEM) of the working microelectrodes and Scanning ElectroChemical Microscopy (SECM) coupled to Atomic Force Microscopy (AFM). The stability of MoS_2 at HER conditions and perspectives of wet-chemical activation of natural or commercially available molybdenite for the (photo)electrochemical water splitting in an acidic medium are discussed.

2. Experimental section

The detailed and illustrated description of all the experimental procedures is given in the Supporting Information, Chapter S1. Here, we provide a brief summary of the experiments.

2.1. Fabrication of top-contacted microelectrodes

The nanofabrication workflow for MoS_2 microelectrodes with the arrays of etching pits surrounded by atomically sharp zigzag edges was based on our pioneering nanopatterning and wet-etching techniques [60]. The nanofabrication steps were performed in the Myfab Nanofabrication Laboratory, MC2 Chalmers. Multilayer MoS_2 flakes were mechanically exfoliated from a 2H-MoS_2 crystal grown by chemical vapor transport (HQ Graphene, the Netherlands; chemical composition and phase structure data are available in Ref. [69]). The flakes were transferred onto 285 nm SiO_2/Si substrates and nanopatterned using a combination of CHF_3-plasma dry etching through an EBL-defined mask and wet etching at 50 – 65°C by a mixture of deionized water, 31% H_2O_2, and 25% NH_3·aq in a 10:1:1 volumetric ratio. 5 nm Cr / 150 nm Au contacts were fabricated by EBL patterning and e-beam metal evaporation, followed by the lift-off process. A *ca.* 1 μm thick poly(methyl methacrylate) (PMMA) insulating layer was used to prevent any electrical contact of metal structures with an electrolyte in subsequent electrochemical experiments. The windows in PMMA were opened by EBL right above the patterned areas of the electrodes to enable highly selective microelectrochemical measurements. The areas above the contact pads near the chip edges were opened as well. Shortly before the electrochemical assessment, the microelectrodes were cleaned for 30 seconds (sec) with 50 W Ar plasma.

2.2. Fabrication of back-contacted microelectrodes

Conductive-through substrates were fabricated for this type of microelectrodes. Silicon dioxide was first removed from the back side of a highly As-doped silicon wafer (resistivity: 0.001 – 0.005 Ω·cm) with buffered oxide etchant (BOE 1:7). Then the wafer was rapidly (60 – 90 sec) placed into an e-beam evaporator, and a 30 nm Ti / 200 nm Au metal layer was deposited. Similarly, an oxide-free face side of the wafer was covered with a 20 nm Ti / 100 nm Au layer. Freshly exfoliated multilayer MoS_2 flakes were transferred to the face-side Au layer (cleaned with 50 W Ar plasma for 2 min) by a single touch to prevent the contamination of the Au-MoS_2 interface. Then, nanohole patterning, dry etching, and wet etching were performed similarly to the top-contacted microelectrodes. No additional contacts were fabricated. Finally, *ca.* 1 μm thick PMMA layer was applied and selectively opened above MoS_2 areas selected for microelectrochemical assessment. Shortly before the electrochemical assessment, the microelectrodes were cleaned for 30 sec with 50 W Ar plasma. Prior to the electrochemical measurements, an additional PDMS film with a 1 – 2 mm wide opening (controlled by optical microscopy) was applied to ensure no contact of the electrolyte with the areas of damaged PMMA resist above the global marks used for EBL alignment.

2.3. Fabrication of the samples for SECM

The samples for SECM were fabricated similarly to back-contacted microelectrodes. However, no thick PMMA layer was applied after the wet etching. Instead, the samples were additionally cleaned for 1 min with 50 W Ar plasma to ensure high cleanliness of the surface.

2.4. Morphological and elemental characterization of the microelectrodes

The facilities of Chalmers Materials Analysis Laboratory (CMAL) and Myfab MC2 Cleanroom were used for the instrumental characterization of MoS_2 flakes and electrodes. Scanning electron microscopy using the Carl Zeiss Ultra 55 microscope was employed to visualize MoS_2 electrodes before and after the microelectrochemical assessment / cycling. The energy-dispersive X-ray spectroscopy (EDS) and elemental mapping of selected samples were performed using Oxford Instruments X-Max 20 mm^2 EDS detector and INCA 4.15 software. In the case of post-electrochemical testing SEM, the electrodes were gently washed with deionized water and thoroughly blow-dried before being loaded into the microscope chamber. Bruker Dimension ICON microscope was used to assess the topography and the local HER activity of the MoS_2 flakes and patterned microelectrodes (see also Chapter 2.6).

2.5. Microelectrochemical assessment

Gamry Reference 600 potentiostat was used for the cyclic voltammetry, linear sweep voltammetry, and open circuit potential measurements of the fabricated microelectrodes. A miniature ("microelectrochemical") setup was assembled to perform three-electrode experiments with the nanofabricated MoS_2 working electrodes. A leakless low-impedance Ag/AgCl electrode was used as a reference electrode. A glassy carbon rod was used as a Pt-free counter electrode. 0.5 M (1 N) H_2SO_4 solution was used as an electrolyte. To prepare it, we used Optima^{TM} grade 98% sulfuric acid with a certified low-ppt concentration of 65 metals (including Pt and PGM), which was diluted with the in-lab produced Milli-Q grade deionized water (resistivity 18.2 MΩ·cm). The electrolyte was purged with N_2 gas for at least 30 min prior to the electrochemical measurements. For the photo-enhanced hydrogen evolution measurements, the microcell was illuminated from the top by a light-emitting diode (LED) white-light source. All the electrochemical measurements were performed at 25°C. Both linear sweep voltammetry (LSV) and cyclic voltammetry (CV) were performed with a 5 mV·sec^{-1} scan rate. All the data is reported without *iR*-drop correction.

2.6. PeakForce SECM

SECM was performed in a substrate generation – tip collection (SG – TG) mode interleaved by the tapping PeakForce scans to get real-time topographical, quantitative nanomechanical, and electrochemical data simultaneously. The electrochemical circuits of the setup were controlled by a bi-potentiostat (CHI920C, CH Instruments, Inc.), while the scanning was performed by Bruker Dimension Icon AFM equipped with standard PeakForce SECM accessories [70]. Nanopatterned MoS_2 flakes on a conductive-through substrate served as a working electrode 1 (WE #1), while Pt tip (Bruker nanoelectrode, 50 nm diameter, fully passivated with SiO_2 except for its apex) acted as a working electrode 2 (WE #2). A lab-made Ag Quasi-Reference Electrode (Ag_{QRE}) was prepared by covering the silver wire with AgCl layers. Pt wire was used as a counter electrode. A low concentration of H_2SO_4 (10 mmol·l^{-1}, pH = 1.7) diluted in KCl supporting electrolyte (100 mmol·l^{-1}) was adopted to limit the formation of H_2 bubbles, which can interfere with the measurement. SECM tip was constantly kept at +150 mV *vs.* Ag_{QRE}. The tip was moved at a lift height of 25 nm over the sample surface to scan the local electrochemical response. Molecular hydrogen, which evolved on the surface of WE #1, was immediately oxidized back to protons at WE #2, enabling the contrast associated with the electrochemical activity of the particular point at WE #1. The scans were performed at 25°C, and WE #1 potentials were set to -200 mV, -300 mV, and -400 mV *vs.* Ag_{QRE}. Interleaved electrochemical and PeakForce tapping scans (providing real-time topography and local mechanical properties data) were performed over a 3 μm × 3 μm surface area at a scan rate of 0.25 Hz. A bare (never etched) MoS_2 flake of similar thickness (50 nm) located on a separate substrate was assessed by AFM-SECM as the reference.

3. Results and discussion

3.1. Edge-enrichment mechanism and electrochemical assessment of top-contacted electrodes

The core idea of MoS_2 edge enrichment employed in this work is based on the fabrication of precisely arranged etching pits surrounded solely by zigzag (*zz*) edges responsible for the electrocatalytic activity. The fabrication protocol includes dry etching by reactive ions (CHF_3 plasma) and subsequent oxidative wet etching by an H_2O_2-based solution (refer to Supporting Information, Chapter S1, for the experimental details). Dry etching creates the initial circular holes precisely defined in the polymer resist by EBL (Supporting Information, Figure S1c). Wet etching is governed by the MoS_2 crystal structure and results in etching pits of triangular or hexagonal symmetry **(Fig. 1**a-d). This is a striking difference from the H_2O_2-based etching of WS_2, which always results in regular hexagonal etching pits [60]. Note that each image in Fig. 1a-d corresponds to the etching pit arrays on different MoS_2 flakes transferred on a single SiO_2/Si chip. Hence, they were etched in precisely the same conditions. The etching pit shapes are the same within a single flake but show a remarkable flake-to-flake variation. We provide an extended description of the wet etching mechanism in the Supporting Information, Chapter S2 [51,53,60–62,71–78]; it is also addressed in our recent publication on second-order nonlinearities at strained MoS_2 *zz* edges [79]. In brief, the employed edge-enrichment technique generates precisely periodic arrays of the etching pits bordered by numerous *zz* edges. In an ideal 2H-MoS_2 polytype with antiparallel S-Mo-S layer stacking, Mo-terminated and S-terminated zigzags (Mo-*zz* and S-*zz*, respectively) are uniformly interlaced along the vertical direction at each wall of the etching pits resulting in a hexagonal shape. Triangular pits are formed due to the certain concentration of the stacking faults and guest polytypes with parallel S-Mo-S layer stacking in the parent 2H-MoS_2 crystal. The hexagonal etching pits contain approximately an equal number of S-*zz* and Mo-*zz* edges, whereas the triangular etching pits exhibit a greater number of one of these edge types. Distinguishing between S-*zz* edges and Mo-*zz* edges in a primarily 2H multilayer structure using electron microscopy is a highly challenging task and exceeds the scope of this study. For conciseness, we will refer to the microelectrodes that have arrays of etching pits with any arrangement of *zz* edges as "edge-enriched". It is also important to note that regardless of the *crystallographic termination type*, the *real structure* of the edges can be composed of guest atoms, like oxygen, and amorphized regions resulting from the oxidative wet etching and the contact with ambient air (even at atmospheric pressure, 25°C). For example, electron energy loss spectroscopy in the STEM regime (STEM-EELS) found an oxygen signal in the edge region of H_2O_2-etched WS_2 [60].

H_2O_2-based etchant is unable to penetrate defect-free MoS_2 basal planes. Consequently, the etching depth in the vertical direction is exclusively determined by dry etching. The completely etched-through pits have circular holes at their centers (Fig. 1a), formed due to the dry etching of the SiO_2/Si substrate. These holes have the same diameter as the ones in MoS_2 before wet etching. When the flake is not completely etched through, it retains MoS_2 layers in the bottom. Several of them are randomly perforated by the CHF_3 plasma. Upon wet etching, these layers are transformed into stepped structures rich in *zz* edges (see also Chapter 3.3).

Fig. 1e shows a schematic cross-section of the top-contacted microelectrodes, while Fig. 1f inset shows the optical image of the exemplary non-patterned and edge-enriched MoS_2 top-contacted electrodes in a final device. The electrochemical activity of the microelectrodes was assessed by linear sweep voltammetry (LSV) in a miniature three-electrode cell using 0.5 M (1 N) H_2SO_4 electrolyte at 25°C (see the Supporting Information, Chapter S1.5 for the details). Fig. 1f shows the polarization curves of a few edge-enriched and non-patterned (basal plane) MoS_2 electrodes. Since the electrocatalyst activity increased with cycles (see Chapter 3.2), we plot here the first measured polarization curves for each electrode to elucidate the effects of nanopatterning. The LSV curves are not *iR*-corrected (see the Supporting Information, Chapter S6 for more details). For the flake with almost hexagonal nanopatterned holes (Fig. 1d), the corresponding non-patterned electrode was irreversibly damaged during the fabrication and could not be assessed. Nevertheless, the other non-patterned electrodes give a reliable dataset for non-patterned MoS_2. Note that the non-patterned electrodes were also in contact with the wet-etching solution because they are located at the very same substrate as the edge-enriched ones. The same colors in Fig. 1f indicate the electrodes fabricated on the same MoS_2 flakes (like in the inset). The edge-enriched electrodes show higher HER activity with good reproducibility of the LSV polarization curves. At -0.78 V_{RHE}, electrochemical current densities (normalized by PMMA window area) are 10.5 – 22.5 mA·cm^{-2} at the non-patterned electrodes (dotted curves) and 156.0 – 175.5 mA·cm^{-2} at the edge-enriched MoS_2 (straight curves). Considering the electrodes fabricated from the same MoS_2 flake, the current density enhancement was 8 – 15 times. HER overpotentials at 1 mA·cm^{-2} (η_1), 10 mA·cm^{-2} (η_{10}), and 100 mA·cm^{-2} (η_{100}) on the edge-enriched and non-patterned electrodes are listed in Table S1. Due to the edge enrichment, η_{10} shows a rather modest decrease of 36 – 132 mV, but η_{100} drops drastically. Edge-enriched electrodes reach 100 mA·cm^{-2} at -752 – -763 mV_{RHE}, while the non-patterned ones cannot reach this current density level even at much more negative potentials.

For a few edge-enriched electrodes, we performed an extended SEM study and estimated the total (three-dimensional) geometric surface area considering the size, shape, and depth of the etching pits, as well as whether they were fully etched through or not. This total area was used to renormalize the measured electrochemical currents (Supporting Information, Figure S5c). Noteworthy, an 8 – 11 times difference between the edge-enriched and non-patterned electrodes in terms of HER current densities at -780 mV_{RHE} is preserved even after this re-normalization. It suggests that the etching pit walls composed of zigzag edges are significantly more electrocatalytically active compared to the MoS_2 basal plane.

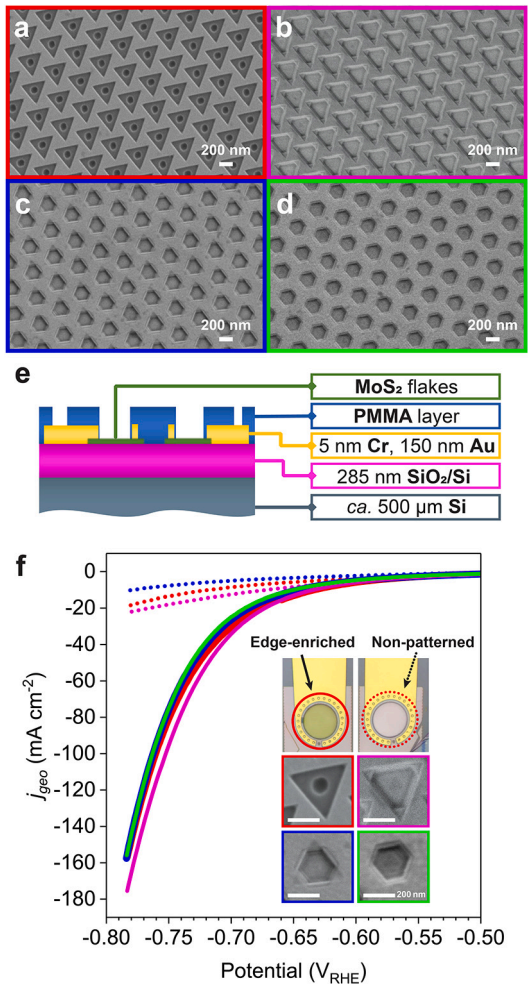

Fig. 1. Crystallography-controlled etching of multilayer MoS_2 flakes and their electrocatalytic activity towards HER. (a-d) SEM micrographs of the pits formed from 100 nm circular holes after wet etching of different MoS_2 flakes located on a single chip and etched at the very same conditions. (e) Schematic cross-section of the top-contacted MoS_2 microelectrodes (not to scale). (f) Polarization curves of the edge-enriched (solid lines) and non-patterned (dotted lines) MoS_2 electrodes. LSV sweep rate is 5 mV·sec^{-1} in 0.5 M O_2-free H_2SO_4 electrolyte, 25°C. Inset 1: An optical micrograph of the top-contacted MoS_2 working electrodes: edge-enriched (straight circle) and non-patterned (dotted circle) ones. Inset 2: Magnified SEM view of the etching pits in the assessed microelectrodes; scale bars are 200 nm. The colors of the polarization curves and frames of SEM images link the electrochemical response to the morphology of the corresponding electrodes. The measured electrochemical currents were normalized by geometric PMMA window area as defined by e-beam lithography; no *iR*-correction was applied. The solid red and blue LSV curves were intentionally made wider than the others to improve their visibility. For the flake with almost regular hexagonal holes, the corresponding non-patterned electrode was irreversibly damaged during the fabrication and could not be assessed. Note that the non-patterned electrodes assessed here were in contact with the wet etching solution. Wider-range LSV curves and the corresponding Tafel plot are shown in the Supporting Information, Figure S5a,b.

The difference between the edge-enriched and non-patterned electrodes is also clearly seen in the Tafel plot (Figure S5b). We found that the studied nanopatterned MoS_2 demonstrates two distinct linear sections in the Tafel plots: one below *ca.* 10 mA·cm^{-2} (TS_{low-j}) and another one between 10 mA·cm^{-2} and 100 mA·cm^{-2} (TS_{high-j}). The corresponding Tafel slopes (TS) are listed in the Supporting Information, Table S1. Interestingly, two distinct linear sections were also observed in the Tafel plots of the NbS_2 electrocatalyst; however, the absolute values were much lower due to the metallic nature of NbS_2 [7]. The TS_{low-j} values of edge-enriched MoS_2 electrodes range within 148 – 178 mV·dec^{-1}. TS_{high-j} is always lower: 105 – 119 mV·dec^{-1}, and close to the TS values reported for MoS_2 etched by water steam (96 mV·dec^{-1}) [46] or a combination of O_2 plasma with NaOCl solution (138 mV·dec^{-1}) [47]. The TS_{low-j} values of the non-patterned electrodes are significantly higher: 192 – 297 mV·dec^{-1}. These electrodes usually cannot provide enough current density to identify the second flat region in the Tafel plot reliably.

We also fabricated a series of identically patterned electrodes on the selected areas of MoS_2 flakes with different thicknesses to vary the total wall area of the triangular and hexagonal etching pits. It was shown that the increase in the total area of etching pit walls composed of *zz* edges results in a continuous decrease of η_{100}, confirming their enhanced electrocatalytic activity (see the Supporting Information, Chapter S3).

3.2. Electrochemical assessment of back-contacted electrodes: effect of electrochemical cycling

To simplify the electrode design and avoid the issues associated with the top-contacting of MoS_2 flakes (see a brief discussion in the Supporting information, Chapter S4 [80–82]), back-contacted microelectrodes were fabricated for further electrochemical studies (**Fig. 2**a and b-inset). Three different types of MoS_2 structures were evaluated: (i) MoS_2 enriched with *zz* edges by dry and wet etching, (ii) MoS_2 with dry-etched circular holes (random set of *zz* and armchair (*ac*) edges), and (iii) bare MoS_2 basal plane never subjected to any etching. Their initial polarization curves are shown in Fig. 2b. In this set of experiments, we scanned the electrodes in the -0.51 – +0.29 V_{RHE} range, starting from the highest and then going to the lowest potential. Hereinafter, we use the following notation to depict the range and scan direction: -0.51 ← +0.29 V_{RHE}; for the cyclic voltammetry (below), it shows the initial direction of the scan. Please refer to the Supporting Information, Chapter S1.5. for the discussion of the open circuit potential and the remarks regarding the CV (and LSV) potential window. Note that MoS_2 was not completely etched through to avoid contact between the electrolyte and the back-contact gold.

The utilization of back-contacted microelectrodes led to a minor improvement of overpotentials: η_{10} decreased from 475 – 483 mV_{RHE} (top-contacted edge-enriched electrodes) to 431 – 450 mV_{RHE} (back-contacted edge-enriched electrodes). The electrode with dry-etched circular holes had roughly the same η_{10} = 445 mV (from the initial LSV). Its polarization curve was nearly identical to the samples that underwent both dry and wet etching (Fig. 2b). The maximum electrochemical current density achieved at -0.51 V_{RHE} (j_{max}) ranged within 2 – 3 mA·cm^{-2}. Meanwhile, the bare MoS_2 electrode, which underwent no etching, exhibited considerably higher current density.

It appears that despite the high concentration of edges in the nanopatterned MoS_2, they are substantially oxidized due to the oxidative H_2O_2-based wet etching (and CHF_3-plasma etching as well) and possibly even due to being stored at ambient conditions in contact with atmospheric oxygen. Therefore, without additional treatment(s), the edge-enriched electrodes seem to be less active than the never etched MoS_2 basal plane (Fig. 2b). However, they were significantly more active than the wet-etched basal plane (see Chapter 3.1). Previously, Voiry et al. [24] reported a significant drop in hydrogen evolution activity upon edge-oxidation of 2H-MoS_2. Electrochemical cycling was shown to be a pathway for partial restoration of the edges' electrocatalytic activity. Similarly, 20 – 40 electrochemical cycles were suggested as good practice before analyzing MoS_2 electrocatalysts [24,68]. Following these recommendations, we applied up to 100 electrochemical cycles to the back-contacted MoS_2 electrodes in the -0.51 ← +0.29 V_{RHE} range. A slow scan rate of 5 mV·sec^{-1} was selected.

Figs. 2c and d show the CV of the MoS_2 microelectrode enriched with *zz* edges. It is clearly seen that its electrocatalytic performance was dramatically enhanced due to cycling. In total, j_{max} increased two orders of magnitude (Fig. 2g), and η_{10} decreased by more than 230

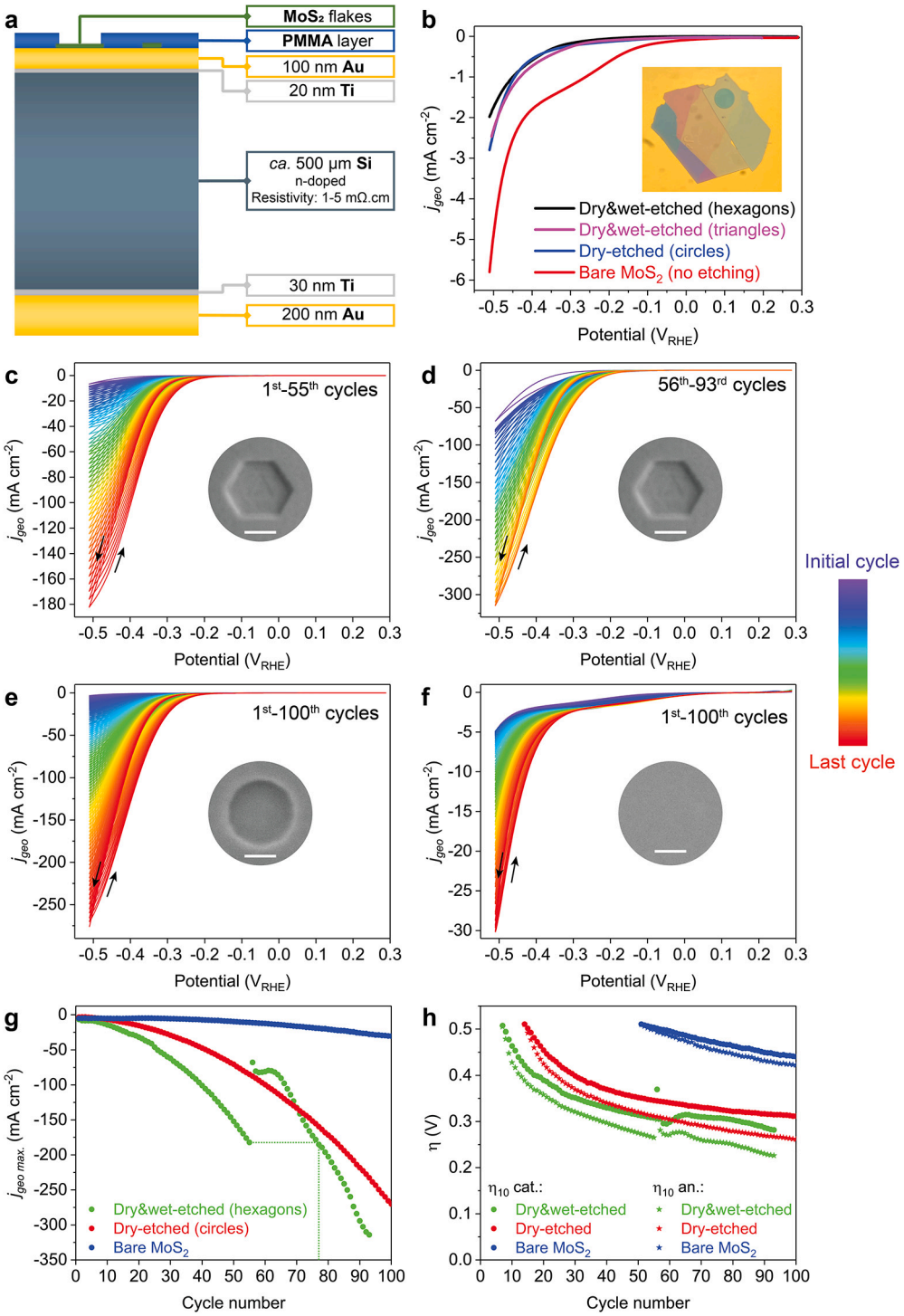

Fig. 2. Electrochemical cycling of the back-contacted MoS_2 microelectrodes. (a) Schematic cross-section of the back-contacted MoS_2 microelectrode (not to scale). (b) Initial LSV curves of the back-contacted MoS_2 electrodes: dry&wet-etched (*zz*-edge-enriched), only dry-etched (circular holes with a random mix of *zz* and *ac* edges), and basal plane MoS_2 without any etching. Inset: An optical top-side micrograph of a typical back-contacted MoS_2 microelectrode. (c, d) CV of the dry&wet-etched electrode (*zz*-edge-enriched) in -0.51 ← +0.29 V_{RHE} range, 5 mV·sec^{-1} scan rate, 25°C: (c) CV curves of 55 cycles before the experiment interruption, (d) CV curves of additional cycles started a few hours after the cycling interruption. (e) CV of only dry-etched electrode (random *zz* and *ac* edge enriched) in -0.51 ← +0.29 V_{RHE} range, 5 mV·sec^{-1} scan rate, 25°C. (f) CV of the bare MoS_2 basal plane electrode without any etching in -0.51 ← +0.29 V_{RHE} range, 5 mV·sec^{-1} scan rate, 25°C. (g) Evolution of j_{max} *vs.* the cycle number for dry&wet-etched, only dry-etched, and bare MoS_2 microelectrodes. (h) Evolution of η_{10} (extracted from cathodic and anodic scans) *vs.* the cycle number for dry&wet-etched, only dry-etched, and bare MoS_2 microelectrodes. The insets in (c-f) show the morphology of the etching pits (if any) in the corresponding electrodes before any electrochemical cycling; the scale bars are 100 nm.

mV (Fig. 2h). After 55 cycles, the experiment was interrupted and continued a few hours later. Interestingly, the activity of the electrode dropped during the interruption period, possibly due to contact with atmospheric oxygen (compare the last cycle in Fig. 2c and the first cycle in Fig. 2d). Once the cycling was continued (with a fresh portion of the electrolyte), electrochemical activity was gradually restored and then enhanced further (Fig. 2g,h).

There are two unusual features in the recorded CV curves to be noted. First, the electrochemical currents during the cathodic (first) scan of each cycle were lower than during the anodic (second) scan of the same cycle (Fig. 2c,d). It means the MoS_2 electrode was more active after being at lower potentials. Second, the hysteresis between cathodic and anodic branches increased with more cycles, and its width reached several tens of mV, although the scan rate was just 5 mV·sec^{-1}. Conversely, most of the other electrocatalyst materials usually exhibit the opposite behavior: anodic scans show lower apparent activity than cathodic ones due to capacitive currents (resulting in just a small hysteresis at low scan rates) and/or poisoning by electrolyte admixtures, absorption of H^+ or H_2, surface reconstruction, *etc.* (resulting in larger hysteresis). However, MXene HER electrocatalysts were also found to have higher activity at anodic scans [83], similar to the nanopatterned MoS_2 in this work. It might be typical for layered materials, although more CV data for other 2D electrocatalysts is required to draw a solid conclusion.

Electrochemical cycling in the -0.51 ← +0.29 V_{RHE} range similarly improves the electrode with only dry-etched circular holes (Fig. 2e). Although the cycling was not interrupted, the j_{max} value achieved after 100 cycles (276 mA·cm^{-2}) was lower than the j_{max} of the dry&wet-etched sample (314 mA·cm^{-2}). In turn, the performance of bare MoS_2 was significantly less improved by the electrochemical cycling (Fig. 2f), although this electrode was more active than nanopatterned ones according to the initial LSV curves (Fig. 2b). The j_{max} increased just about 5 – 6 times after the same 100 cycles (Fig. 2g), η_{10} decreased noticeably less than for the nanopatterned electrodes, and η_{100} was never reached within the cycling range (Fig. 2h). Significantly less pronounced activation of the MoS_2 basal plane electrodes highlights the beneficial effect of the nanopatterning on the HER performance of MoS_2 microelectrodes. Also, it rules out the potentially suspected metals deposition from the electrolyte at low potentials. Also, note that the cycling experiments were performed using the ultra-clean H_2SO_4 electrolyte with a low-ppt level of metal concentration. A glassy carbon counter electrode was used to avoid any metal contamination of the electrolyte, which is typical for Pt counter electrodes.

The evolution of electrocatalytic activity descriptors upon cycling of the *zz*-edge-enriched electrode deserves a more detailed discussion. An additional plot of η_1, η_{10}, and η_{100} (from cathodic and anodic scans) *vs.* the cycle number is shown in the Supporting Information, Figure S9a. The η_{10} and η_{100} values first decreased rapidly and then were gradually saturating. η_1 showed mixed trends during a few initial cycles but then resembled the evolution of η_{10} and η_{100} (Supporting Information, Figure S9a). Conversely, j_{max} changed slowly within the first 10 cycles, and then its growth was accelerated without any saturation (Fig. 2g). Similar trends were observed upon cycling of the microelectrode with dry etched circular holes (Supporting Information, Figure S9b).

When cycling of dry&wet-etched microelectrode was interrupted and then resumed, j_{max} dropped dramatically and almost did not change during a few cycles like at the very beginning of the experiment, *i.e.*, the electrode partially "lost memory" about the previous cycling (Fig. 2g). In contrast, during the 57^{th} – 63^{rd} cycles when j_{max} was almost unchanged, the η_1 and η_{10} restored rapidly and even reached smaller values (especially η_1) than before the interruption (Supporting Information, Figure S9a). The j_{max} value achieved at the 55^{th} cycle (right before the cycling interruption) was restored only at the 77^{th} cycle (Fig. 2g). Surprisingly, a clear bending of the j_{max} curve can be seen near this cycle (Supporting Information, Figure S9b). The fluctuations of η_1, η_{10}, and η_{100} also stabilized by this moment, and they started to decrease continuously (Supporting Information, Figure S9a). It turns out that the electrode still had some "memory" of the activity level to which it was cycled previously. Such dynamics of η_1, η_{10}, η_{100}, and j_{max} suggests that at least two types of changes occurred in the system with different rates. We hypothesize that the following interrelated groups of processes could contribute to the enhanced electrocatalytic activity:

1. (Electro)chemical reduction of the oxidized edge atoms and atomic-level edge reconstruction.

2. Nano- and micro-scale morphology changes, including the surface roughening and evolution of the etching pits' shape.

The first group of processes is challenging to track directly in the nanopatterned microelectrodes. They are smaller than the sampling area of state-of-the-art micro-area X-ray photoelectron spectrometers. Also, these changes significantly deteriorate once the cycling is stopped, possibly due to fast edge oxidation. High-resolution and high-sensitivity *operando* techniques might be used to study these effects in the future. Conversely, the second group of processes, the electrode morphology evolution, is easier to track using *ex-situ* SEM and will be discussed below in detail.

Electrochemical cycling of another *zz*-edge-enriched electrode in the -0.3 ← +0.2 V_{RHE} range revealed that going to either low absolute potentials or relatively high current densities is important to reach a significant improvement of MoS_2 activity by electrochemical cycling (see the Supporting Information, Chapter S5).

After completing the electrochemical cycling, the electrodes were analyzed by SEM. **Fig. 3**b shows the *ex-situ* micrograph of the *zz*-edge-enriched electrode after 100 electrochemical cycles in the -0.51 ← +0.29 V_{RHE} range (Fig. 2c,d). Obviously, the etching pits are significantly modified, and their edges are not as sharp anymore. Instead, the finger-like nanostructures seem to stay between the former walls of the etching pits and the remaining distorted nanoribbons of the honeycomb pattern (Fig. 3b). Similar but milder changes were observed in the electrode cycled in the -0.3 ← +0.2 V_{RHE} range (Fig. 3d-f). Apparently, the electrochemical reduction of edge atoms (the first group of processes mentioned above) and the enhancement of electrocatalytic activity upon cycling are accompanied by the significant evolution of electrode morphology (the second group of processes). Interestingly, the electrode cycled in the -0.3 ← +0.2 V_{RHE} range initially had triangular etching pits (see the mechanism explanation in Supporting Information, Chapter S2). After cycling, they were converted into distorted hexagons. Fig. 3f shows the overlapped images of the initial (triangular) and the final (hexagonal) etching pits. Obviously, the finger-like structures propagate all the way from the location of the triangular etching pit wall to the hexagon's walls. Conversely, the vertices of triangles are converted into relatively sharp edges of the hexagons. In contrast, when the initial shape of the etching pits was almost hexagonal (Fig. 3a), all the walls of the electrochemically-evolved hexagon contained rough "fingers" (Fig. 3c). It might indicate that in the reducing conditions of hydrogen evolution reaction, the relative stabilities of Mo-*zz* and S-*zz* edges are changed and (possibly) even inversed as compared to the H_2O_2-based wet etching environment (also see the Supporting Information, Chapter S2).

The morphological evolution of the dry-etched sample upon electrochemical cycling is shown in Fig. 3g-i: the initial circular holes were converted into rounded triangles with rough walls. Obviously, the morphological evolution of the circular holes upon electrochemical cycling is also governed by the MoS_2 crystal structure. Overall, the presence of initial well-defined and atomically sharp features on the surfaces of nanopatterned electrodes strongly facilitated the tracking of their morphological changes in electrochemical experiments. We also benefited from the small microelectrode dimensions and its precisely defined location on the chip, which enabled *ex-situ* SEM study of the same electrode areas *before* and *after* microelectrochemical assessment. These are significant advantages of our research methodology compared to the previous reports, which tracked the stability of MoS_2-based HER electrocatalysts *via* overall electrochemical performance assessment, X-ray

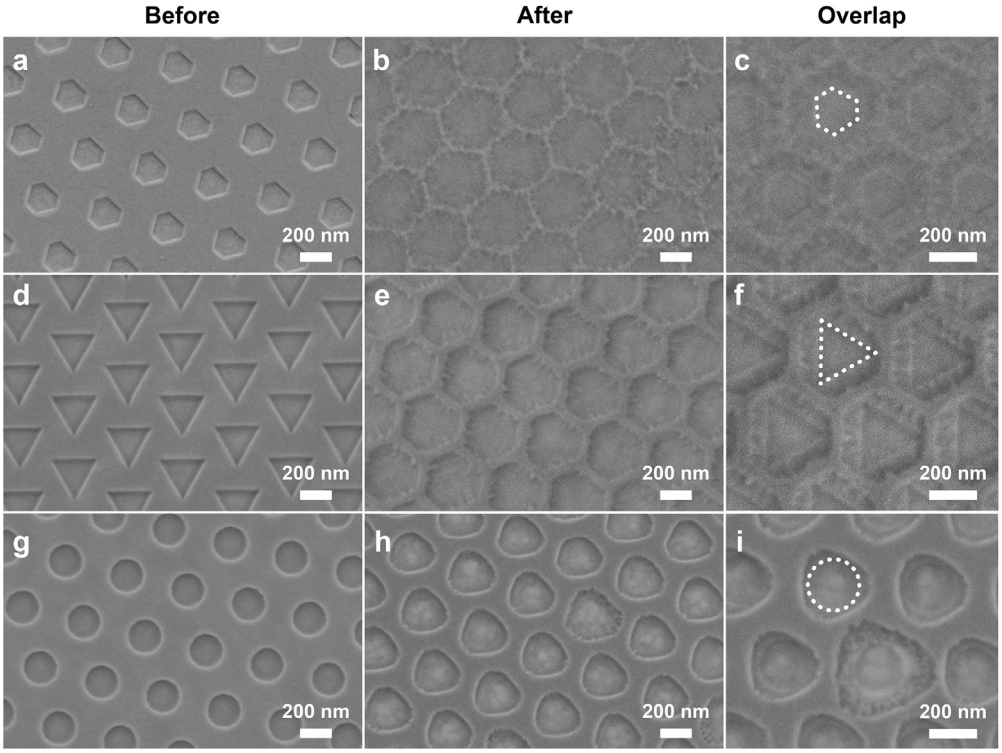

Fig. 3. Tracking morphological evolution of the MoS_2 electrodes due to the electrochemical cycling using *ex-situ* SEM. (a-c) Dry&wet-etched electrode (zigzag-edge-enriched distorted hexagons) before and after 100 electrochemical cycles in the -0.51 ← +0.29 V_{RHE} range, 5 $mV{\cdot}sec^{-1}$ scan rate. (d-f) Dry&wet-etched electrode (zigzag-edge-enriched triangles) before and after 50 electrochemical cycles in the -0.3 ← +0.2 V_{RHE} range, 5 $mV{\cdot}sec^{-1}$ scan rate. (g-i) Dry-etched electrode (circular holes with random edges) before and after 100 electrochemical cycles in the -0.51 ← +0.29 V_{RHE} range, 5 $mV{\cdot}sec^{-1}$ scan rate. (a, d, g) – the electrodes before electrochemical cycling; (b, e, h) – the same electrodes after the corresponding electrochemical cycling; (c, f, i) – magnified and artificially overlapped images of the few etching pits before and after the above-mentioned electrochemical cycling. In each overlapped image, the shape of a single initial etching pit (before the electrochemical cycling) is outlined by a dotted line for clarity.

photoelectron spectroscopy (XPS), or electron microscopy of arbitrary areas of large polycrystalline electrodes. Note that special precautions were taken to eliminate potential carbon contamination caused by SEM before electrochemical measurements (Supporting Information, Chapter S1.4.).

Together with electrochemical data, the observed morphological changes may indicate that MoS_2 shows a self-optimizing behavior and generates the most appropriate sites for HER. However, significant degradation of the surface after prolonged cycling may indicate that the HER-active sites in MoS_2 are not stable enough, and the observed enhancement of electrocatalytic activity is unavoidably accompanied by the self-sacrifice of the material. This behavior might be specific for 2D materials enriched with zigzag edges *via* oxidative wet etching, which has been gaining popularity in the last years [46,47,51]. Many of our single-particle electrodes suffered from breakdown/puncturing when the cycling was prolonged beyond 100 cycles (for example, see Supporting Information, Figure S11). The degradation seems to be accelerated at random defects, which can concentrate the electrical field and/or dissolve faster. Notably, j_{max} continued to increase without visible saturation until the breakdown point. Although the major part of the *electrocatalyst* in the punctured electrodes is still relatively intact, such *devices* give incorrect electrochemical readouts due to the direct contact between the underlying gold and electrolyte. It seems that it is an essential limitation of the single-particle 2D electrodes. However, we carefully checked that all the data reported in this article were collected *before* any breakdown of the devices and, therefore, represent the signal from MoS_2 surface only.

Previously, it was suggested that the electrochemical cycling of oxidized 2H-MoS_2 could partially restore MoS_2 nanosheets and their edges. For instance, XPS confirmed a progressive decrease of the Mo^{6+} signal with more cycles applied [24]. However, our results may indicate that the oxidized edges are gradually removed and, in this way, "converted" into not-oxidized edges rather than restored to the initial state. This pathway also looks more realistic, considering the absence of any sulfur and/or molybdenum supply into the electrochemical cell.

In an additional experiment, we kept a freshly fabricated dry&wet-etched MoS_2 electrode under 0.5 M H_2SO_4 solution without connecting the potentiostat leads. The experiment continued for 10 hours, the typical duration of our CV experiments with a 5 $mV{\cdot}sec^{-1}$ scan rate. SEM checks before and after the treatment with H_2SO_4 revealed no noticeable changes in the microelectrode morphology (Supporting Information, Figure S12). Thus, some redox reactions governed by the applied potentials rather than exchange reactions between strong sulfuric acid and the disulfide compound seem to be responsible for the gradual electrochemical dissolution of MoS_2. Alternatively, proton intercalation and formation of hydrogen nanobubbles may lead to the perforation and exfoliation of MoS_2, as suggested elsewhere [66]. Since we observe the crystallography-governed morphological evolution of the etching pits, electrochemical redox reactions seem to be involved in edge dissolution. However, the appearance of the ruptured etching pit walls may suggest that the hydrogen nanobubbles can also make an impact. On top of that, the destructive thermal impact caused by local heating upon running current through the poorly conductive electrode cannot be ruled out.

After the electrochemical cycling, our nanopatterned MoS_2 electrodes enriched with *zz* edges (dry&wet etching) or random edges (dry etching) showed one of the best overpotential and TS values compared to the other top-down activated MoS_2 powders and mechanically exfoliated flakes. We illustrate this in **Fig. 4** by comparing η_{10} and TS values from different top-down activated MoS_2 electrocatalysts. The extended considerations regarding the achieved absolute overpotential values are provided in the Supporting information, Chapter S6 [84–88]).

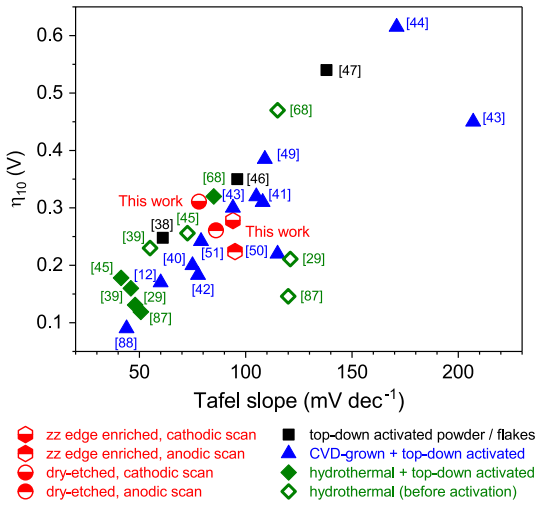

Fig. 4. A map of the electrochemical activity for the top-down activated MoS_2 electrocatalysts, listed in the Supporting Information, Table S2, and discussed in Chapter S6. The η_{10} and Tafel slope values were used as the key numerical descriptors to plot the map.

Additional LSV measurements under white-light illumination (Supporting information, Figure S13a) prompted a future potential of *zz*-edge-enriched MoS_2 electrodes for photo-enhanced hydrogen evolution. A *zz*-edge-enriched electrode treated by 50 electrochemical cycles was used for this experiment. Figure S13b (Supporting Information) shows the LSV polarization curve (red) registered when the cell was illuminated with a 100 mW white-light source; the curves in the darkness right before (black) and after (blue) illumination were also registered for comparison. Applying the white-light illumination resulted in a 7.5-fold increase of electrochemical current density at -0.5 V_{RHE} (j_{max}): from 4.5 mA·cm^{-2} to 33.8 mA·cm^{-2}. At the same time, η_{10} shifted from -407 mV_{RHE} to -342 mV_{RHE}. Obviously, the white light generates electron-hole pairs in MoS_2, which has *ca.* 1.2 eV indirect bandgap and *ca.* 1.95 eV direct bandgap [89]. As a result, the electrical conductivity of the semiconductor electrode is increased. The photo-gating effect can also improve MoS_2 conductivity [78], while photo-generated electrons can directly participate in proton reduction as well. Remarkably, after switching off the illumination, the electrode showed a j_{max} of 8.3 mA·cm^{-2}. Such a huge jump in the j_{max} (almost twice) was never observed within just a couple of electrochemical cycles without illumination (see Fig. 2). This may suggest that running higher current densities through the electrode is more important for the electrocatalytic activity enhancement than only applying negative potentials.

In the future, the *zz*-edge-enriched MoS_2 electrodes can be used as the active support for platinum particles, leading to the low-Pt-loaded MoS_2 electrocatalysts as reported elsewhere [50]. Ultrasharp zigzag edges nanofabricated here might be ideal sites for Pt nanocrystal growth similar to gold nanoparticles (see Refs. [90–92] and the Supporting Information, Figure S14).

3.3. Scanning electrochemical microscopy of the individual hexagonal etching pits in MoS_2

SECM was the second highly localized electrochemical technique that we used to map HER activity of *zz*-edge-enriched MoS_2. Local electrochemical investigations of MoS_2 electrocatalytic activity have been gaining popularity in the recent decade. However, they are mostly limited to "as is" exfoliated or CVD-grown MoS_2 rather than deterministically patterned electrodes. For instance, micropipette-based scanning electrochemical cell microscopy (SECCM) was employed to visualize the enhanced hydrogen evolution activity of edges, steps, and crevices of mechanically exfoliated MoS_2 flakes as compared to the basal plane [93–95]. SECCM was also used to study the photoelectrochemical oxidation of CVD-grown MoS_2 monolayer at positive potentials [96] and quantify the electrochemical H_2 bubble nucleation on the MoS_2 surface [97]. Active sites of CVD-grown MoS_2 nanosheets and MoS_2/WS_2 hetero-nanosheets were mapped in the voltammetric hopping mode of SECCM, with the probe's tip diameter of 40-95 nm [98]. Scanning electrochemical microscopy (SECM) is another powerful modality for studying the electrochemical responses at the micro- and nano-level. When coupled with AFM, it allows simultaneous acquisition of electrochemical, topographical, and mechanical information about the electrocatalyst [70,99]. SECM was previously used to map electron transfer kinetics of MoS_2 in a feedback mode [100–103] and directly map HER activity in substrate generation – tip collection mode [102–104]. These studies unequivocally confirmed the enhanced electrochemical activity of metallic 1T-MoS_2 polytype [102] along with the edges/steps [100,102] and sulfur vacancies in 2H-MoS_2 [103,104]. PeakForce AFM-SECM also revealed rich band alignment effects in the MoS_2-liquid interface depending on the layer number and thickness of CVD-grown MoS_2 [101]. In the present research, SECM coupled to AFM (PeakForce mode [70]) was used for simultaneous mapping of the hydrogen evolution active sites, topography, and intrinsic properties of the patterned edge-enriched MoS_2.

SECM was performed in substrate generation – tip collection (SG – TC) mode where HER occurred on the surface of the substrate (working electrode #1) while hydrogen oxidation reaction (HOR) occurred on the AFM-SECM nanotip (working electrode #2) [105]. The working electrode #1 (*i.e.*, patterned MoS_2) was fabricated similarly to the back-contacted ones used in microelectrochemical three-electrode measurements, but no polymer resist layer was applied after wet etching. Also, the individual *zz*-edge-enriched etching pits were studied instead of the etching pit arrays.

Fig. 5 summarizes the AFM-SECM assessment of an individual *ca.* 2 μm hexagonal etching pit in MoS_2. Note that the pit was not completely etched through to avoid unwanted signals from the Au back contact. The tip – substrate adhesion signal was considered a "chemical" mapping of the substrate because any force between the tip and the substrate was affected by the chemistry of the latter. Thus, Fig. 5 represents the local evolution of the topography, chemistry, and electroactivity of the patterned MoS_2 at the potentials of -200, -300, and -400 mV *vs.* lab-made Ag Quasi-Reference Electrode at 25°C. Note that the presented hexagonal etching pit (Fig. 5a) was dry&wet-etched. Basal surfaces around the etching pit were protected by ARP resist during dry etching (see Supporting Information, Chapters S1.1-S1.3) but were in contact with the wet-etching mixture afterward. For comparison, we also collected AFM-SECM maps of a bare (never etched) MoS_2 flake of identical thickness (50 nm) located at a separate substrate; these maps are shown in the Supporting information, Figure S15. For better comparison of the AFM-SECM data, we also plotted the averaged horizontal line scans for height, adhesion, and HOR current at the nanotip (Figs. 5j, k, and l, respectively).

Figs. 5b, e, and h show a slight variation of the tip – substrate adhesion, highlighting the chemical modification of MoS_2 composition locally at the edge of the etching pit. A pronounced electrochemical signal (*i.e.*, HOR current at the 50 nm tip) was detected from the bottom of the hexagonal etching pit even at -200 mV_{AgQRE}, while the basal surface around was almost inactive (Fig. 5c). At higher overpotentials (*i.e.*, more negative potentials), HOR current above the hexagon bottom increased noticeably, while a near-zero signal of the surrounding MoS_2 basal surface remained almost unchanged (Fig. 5c, f, and i). The comparison of average horizontal line scans for topography and HOR current (Figs. 5j and l) shows that the electrochemical activity is maximum in the hexagonal etching pit (its projection is highlighted in pale yellow in Figs. 5j, k, and l). At the same time, the basal surfaces around the etching pit and the bare (never etched) MoS_2 reference showed negligible average HOR current. As discussed above, the bottom of the initial circular holes, which were not completely etched through by

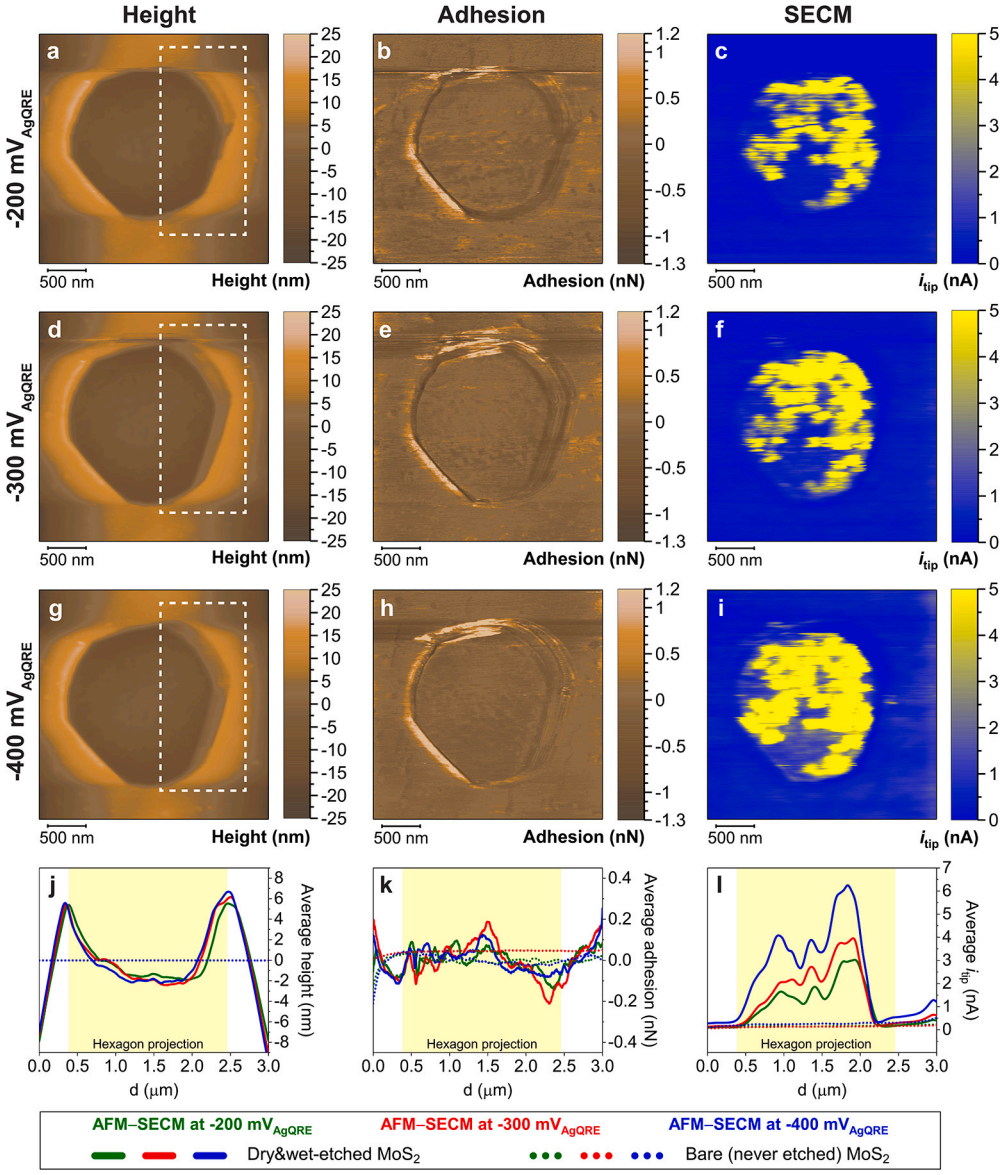

Fig. 5. PeakForce AFM-SECM of an individual *ca.* 2 μm hexagonal etching pit in MoS_2. (a, d, g) – height profile, (b, e, h) – adhesion profile, (c, f, i) – electrochemical current at the SECM tip (i_{tip}) corresponding to the real-time oxidation of the H_2 molecules evolved at the nanopatterned MoS_2 microelectrode at the potentials of -200 mV_{AgQRE}, -300 mV_{AgQRE}, and -400 mV_{AgQRE}, respectively (25°C). (j, k, l) – the average height, adhesion, and i_{tip} profiles, respectively. These profiles are obtained by averaging all the horizontal line scans of the given signal at the given potential applied to the MoS_2 microelectrode. The projection of the hexagonal etching pit to the horizontal axis is highlighted in pale yellow in panes j, k, and l. The signals of dry&wet-etched MoS_2 (solid lines) inside the pale-yellow areas correspond mainly to the hexagonal etching pit. The same curves outside the hexagon projection represent MoS_2 basal surfaces, which were protected by ARP resist during dry etching but were in contact with the wet-etching mixture afterward. The dotted lines represent the average horizontal profiles of bare (never etched) MoS_2 flake (see the corresponding AFM-SECM maps in the Supporting Information, Figure S15).

CHF_3 plasma, contained a few MoS_2 layers randomly perforated with the reactive ions. Obviously, wet etching generates *zz*-edge-enriched structures in these layers as well. Small triangle- and hexagon-shaped features can be seen at the bottom of the etching pits in the inset of Fig. 1f. In an additional experiment for better visualization, we decorated large hexagonal pits (incompletely etched in the vertical direction) with gold nanoparticles *via* a spontaneous reaction with $HAuCl_4$. Au nanoparticles deposited using this technique are known to highlight the surface defects of MoS_2 and WS_2 nanostructures [90,91]. As seen in Figure S14, the hexagonal etching pit bottoms were densely populated with the stepped patterns that followed the *zz* directions of the flake. A much lower density of Au nanoparticles was observed in the basal surface around the etching pits. The dense *zz* edge sites at the bottom of the hexagonal etching pit were responsible for the increased HER activity in this area. Surprisingly, some areas near the hexagon walls remained less active than the etching pit. In addition, these areas underwent noticeable morphological changes, as most clearly seen from the topology (height) signal (see the areas highlighted by dashed lines in Figs. 5a, d, and g). It seems that here, we directly observed the shape evolution of the etching pit, similar to that which manifested upon the prolonged electrochemical cycling and was associated with a strong enhancement of the MoS_2 electrocatalytic activity (see Chapter 3.2). A drop in the hydrogen evolution signal in these very areas may argue for the competitive electrochemical reactions to be responsible for the morphological evolution of the electrode.

4. Conclusions

A combination of a dry etching by CHF_3 plasma and H_2O_2-based wet etching was shown to be a feasible pathway toward the determin-

istic fabrication of multilayer MoS_2 microelectrodes with dense arrays of triangular or hexagonal etching pits bordered with numerous zigzag edges. These electrodes were thoroughly assessed by two highly localized electrochemical techniques: three-electrode microelectrochemical measurements with precisely defined regions of electrode-electrolyte contact and PeakForce scanning electrochemical microscopy. Upon electrochemical cycling in an acidic electrolyte, the electrocatalytic hydrogen evolution activity of such electrodes was dramatically enhanced: the electrochemical current density achieved at -510 mV_{RHE} (j_{max}) was increased by two orders of magnitude. Meanwhile, the pristine MoS_2 basal plane showed just about 6 times j_{max} increase after the very same cycling. After cycling, the zigzag-edge-enriched electrode required η_{10} = 282 mV and η_{100} = 389 mV overpotential to reach 10 $mA{\cdot}cm^{-2}$ and 100 $mA{\cdot}cm^{-2}$ electrochemical current densities, respectively. Noticeably, during the cycling, a significant hysteresis developed between the cathodic (first) and anodic (second) branches of CV curves. In the anodic curve, the activity of the electrode was higher than in the cathodic curve: η_{10} = 226 mV and η_{100} = 355 mV values were achieved. The enhanced electrochemical activity was attributed to the electrochemical reduction of active sites located at the zigzag edges of the material. This phenomenon was accompanied by notable degradation of the electrode morphology, which was accurately studied by *ex-situ* SEM. It was hypothesized that the activity of MoS_2 zigzag edges is partially sacrificial and may compromise the long-term stability of MoS_2 electrocatalysts, at least when they are fabricated by top-down oxidative techniques. SECM additionally demonstrated the pronounced hydrogen evolution activity in the bottoms of hexagonal etching pits densely populated with stepped zigzag edges. The intense white light illumination significantly boosted the hydrogen evolution activity of zigzag-edge-enriched MoS_2 electrodes. Our study sheds light on significant opportunities and challenges of the top-down activation of multilayer MoS_2 crystals crucial for the scalable application of this Pt-free electrocatalyst in the future hydrogen economy.

CRediT authorship contribution statement

Alexander Yu. Polyakov: Writing – review & editing, Writing – original draft, Methodology, Validation, Investigation, Formal analysis, Conceptualization, Visualization. **Serge Al Bacha:** Writing – review & editing, Writing – original draft, Methodology, Validation, Investigation, Formal analysis, Visualization. **Waleed M.A. El Rouby:** Writing – review & editing, Methodology, Investigation, Validation. **Battulga Munkhbat:** Writing – review & editing, Methodology, Conceptualization. **Loïc Assaud:** Writing – review & editing, Methodology, Validation. **Pierre Millet:** Writing – review & editing, Supervision, Resources, Methodology, Validation, Funding acquisition. **Björn Wickman:** Writing – review & editing, Supervision, Resources, Methodology, Validation, Conceptualization. **Timur O. Shegai:** Writing – review & editing, Validation, Supervision, Resources, Project administration, Methodology, Funding acquisition, Conceptualization.

Declaration of competing interest

The authors declare that they have no known competing financial interests or personal relationships that could have appeared to influence the work reported in this paper.

Data availability

The data supporting the findings of this study are available on request from the corresponding authors: AYP and TOS.

Acknowledgements

The authors thank 2D-TECH – Vinnova competence center for the financial support of this work (Ref. 2019-00068). This work was performed in part at Myfab Chalmers and the Chalmers Material Analysis Laboratory, CMAL. The authors thank Patrik Bjöörn and Simon Torell (Smena Catalysis AB, Sweden) for establishing collaboration between Elogen, SMENA Catalysis AB, Chalmers University of Technology, and the University of Paris-Saclay, as well as for the discussions of the commercial potential of MoS_2 electrocatalysts. The authors thank Dr. Georgii Zograf, Dr. Gerard Montserrat-Sisó, Dr. Adriana Canales, Dr. Alok Ranjan, Dr. Oliver Olsson, Prof. Andreas Dahlin, Dr. Ruggero Verre, Dr. Abhay V. Agrawal, Dr. Betül Küçüköz (Chalmers University of Technology, Sweden), and Dr. Alexander Vaskevich (Weizmann Institute of Science, Israel) for the help with some experiments and fruitful discussions.

Appendix A. Supplementary material

Supplementary material related to this article can be found online at https://doi.org/10.1016/j.mtnano.2024.100467.

References

[1] P. Millet, PEM water electrolysis, in: A. Godula-Jopek, D. Stolten (Eds.), Hydrogen Production, Wiley-VCH Verlag GmbH & Co. KGaA, 2015, pp. 63–116, https://doi.org/10.1002/9783527676507.ch3.
[2] N. Guillet, P. Millet, Alkaline water electrolysis, in: A. Godula-Jopek, D. Stolten (Eds.), Hydrogen Production, Wiley-VCH Verlag GmbH & Co. KGaA, 2015, pp. 117–166, https://doi.org/10.1002/9783527676507.ch4.
[3] D. Bessarabov, P. Millet, PEM Water Electrolysis, Academic Press, San Diego, CA, 2018.
[4] J. Zhu, L. Hu, P. Zhao, L.Y.S. Lee, K.-Y. Wong, Recent advances in electrocatalytic hydrogen evolution using nanoparticles, Chem. Rev. 120 (2) (2019) 851–918, https://doi.org/10.1021/acs.chemrev.9b00248.
[5] S. Li, B. Fei, Two-dimensional transition metal-based electrocatalyst and their application in water splitting, Mater. Sci. Technol. 38 (9) (2022) 535–555, https://doi.org/10.1080/02670836.2022.2062644.
[6] H. Wu, C. Feng, L. Zhang, J. Zhang, D.P. Wilkinson, Non-noble metal electrocatalysts for the hydrogen evolution reaction in water electrolysis, Electrochem. Energy Rev. 4 (3) (2021) 473–507, https://doi.org/10.1007/s41918-020-00086-z.
[7] J. Yang, A.R. Mohmad, Y. Wang, R. Fullon, X. Song, F. Zhao, I. Bozkurt, M. Augustin, E.J.G. Santos, H.S. Shin, W. Zhang, D. Voiry, H.Y. Jeong, M. Chhowalla, Ultrahigh-current-density niobium disulfide catalysts for hydrogen evolution, Nat. Mater. 18 (12) (2019) 1309–1314, https://doi.org/10.1038/s41563-019-0463-8.
[8] T.F. Jaramillo, K.P. Jørgensen, J. Bonde, J.H. Nielsen, S. Horch, I. Chorkendorff, Identification of active edge sites for electrochemical H_2 evolution from MoS_2 nanocatalysts, Science 317 (5834) (2007) 100–102, https://doi.org/10.1126/science.1141483.
[9] B. Hinnemann, P.G. Moses, J. Bonde, K.P. Jørgensen, J.H. Nielsen, S. Horch, I. Chorkendorff, J.K. Nørskov, Biomimetic hydrogen evolution: MoS_2 nanoparticles as catalyst for hydrogen evolution, J. Am. Chem. Soc. 127 (15) (2005) 5308–5309, https://doi.org/10.1021/ja0504690.
[10] Q. Ding, B. Song, P. Xu, S. Jin, Efficient electrocatalytic and photoelectrochemical hydrogen generation using MoS_2 and related compounds, Chem 1 (5) (2016) 699–726, https://doi.org/10.1016/j.chempr.2016.10.007.
[11] F.M. Pesci, M.S. Sokolikova, C. Grotta, P.C. Sherrell, F. Reale, K. Sharda, N. Ni, P. Palczynski, C. Mattevi, MoS_2/WS_2 heterojunction for photoelectrochemical water oxidation, ACS Catal. 7 (8) (2017) 4990–4998, https://doi.org/10.1021/acscatal.7b01517.
[12] H. Li, C. Tsai, A.L. Koh, L. Cai, A.W. Contryman, A.H. Fragapane, J. Zhao, H.S. Han, H.C. Manoharan, F. Abild-Pedersen, J.K. Nørskov, X. Zheng, Activating and optimizing MoS_2 basal planes for hydrogen evolution through the formation of strained sulphur vacancies, Nat. Mater. 15 (1) (2015) 48–53, https://doi.org/10.1038/nmat4465.
[13] J. Xu, G. Shao, X. Tang, F. Lv, H. Xiang, C. Jing, S. Liu, S. Dai, Y. Li, J. Luo, Z. Zhou, Frenkel-defected monolayer MoS_2 catalysts for efficient hydrogen evolution, Nat. Commun. 13 (1) (2022) 2193, https://doi.org/10.1038/s41467-022-29929-7.
[14] Y.M. Ding, N.W. Li, S. Yuan, L. Yu, Surface and interface engineering strategies for MoS_2 towards electrochemical hydrogen evolution, Chem., Asian J. 17 (14) (2022) e202200178, https://doi.org/10.1002/asia.202200178.
[15] Z.W. Seh, J. Kibsgaard, C.F. Dickens, I. Chorkendorff, J.K. Nørskov, T.F. Jaramillo, Combining theory and experiment in electrocatalysis: insights into materials design, Science 355 (6321) (2017) eaad4998, https://doi.org/10.1126/science.aad4998.
[16] J.D. Benck, T.R. Hellstern, J. Kibsgaard, P. Chakthranont, T.F. Jaramillo, Catalyzing the hydrogen evolution reaction (HER) with molybdenum sulfide nanomaterials, ACS Catal. 4 (11) (2014) 3957–3971, https://doi.org/10.1021/cs500923c.
[17] C. Sun, L. Wang, W. Zhao, L. Xie, J. Wang, J. Li, B. Li, S. Liu, Z. Zhuang, Q. Zhao, Atomic-level design of active site on two-dimensional MoS_2 toward efficient hydrogen evolution: experiment, theory, and artificial intelligence modelling, Adv. Funct. Mater. 32 (38) (2022) 2206163, https://doi.org/10.1002/adfm.202206163.

[18] Y. Cheng, H. Song, H. Wu, P. Zhang, Z. Tang, S. Lu, Defects enhance the electrocatalytic hydrogen evolution properties of MoS_2-based materials, Chem., Asian J. 15 (20) (2020) 3123–3134, https://doi.org/10.1002/asia.202000752.
[19] D. Voiry, R. Fullon, J. Yang, C. de Carvalho Castro e Silva, R. Kappera, I. Bozkurt, D. Kaplan, M.J. Lagos, P.E. Batson, G. Gupta, A.D. Mohite, L. Dong, D. Er, V.B. Shenoy, T. Asefa, M. Chhowalla, The role of electronic coupling between substrate and 2D MoS_2 nanosheets in electrocatalytic production of hydrogen, Nat. Mater. 15 (9) (2016) 1003–1009, https://doi.org/10.1038/nmat4660.
[20] B. Chen, J. Wang, S. He, Y. Shen, S. Huang, H. Zhou, Fabrication of cos_2-mos_2 heterostructure via interface engineering toward efficient dual-pH hydrogen evolution, J. Alloys Compd. 948 (2023) 169655, https://doi.org/10.1016/j.jallcom.2023.169655.
[21] J. Feng, H. Zhou, D. Chen, T. Bian, A. Yuan, Core-shell structured ZnCo/NC@MoS_2 electrocatalysts for tunable hydrogen evolution reaction, Electrochim. Acta 331 (2020) 135445, https://doi.org/10.1016/j.electacta.2019.135445.
[22] H. Wang, Z. Lu, D. Kong, J. Sun, T.M. Hymel, Y. Cui, Electrochemical tuning of MoS_2 nanoparticles on three-dimensional substrate for efficient hydrogen evolution, ACS Nano 8 (5) (2014) 4940–4947, https://doi.org/10.1021/nn500959v.
[23] H. Wang, Z. Lu, S. Xu, D. Kong, J.J. Cha, G. Zheng, P.-C. Hsu, K. Yan, D. Bradshaw, F.B. Prinz, Y. Cui, Electrochemical tuning of vertically aligned MoS_2 nanofilms and its application in improving hydrogen evolution reaction, Proc. Natl. Acad. Sci. 110 (49) (2013) 19701–19706, https://doi.org/10.1073/pnas.1316792110.
[24] D. Voiry, M. Salehi, R. Silva, T. Fujita, M. Chen, T. Asefa, V.B. Shenoy, G. Eda, M. Chhowalla, Conducting MoS_2 nanosheets as catalysts for hydrogen evolution reaction, Nano Lett. 13 (12) (2013) 6222–6227, https://doi.org/10.1021/nl403661s.
[25] Y. Yin, J. Han, Y. Zhang, X. Zhang, P. Xu, Q. Yuan, L. Samad, X. Wang, Y. Wang, Z. Zhang, P. Zhang, X. Cao, B. Song, S. Jin, Contributions of phase, sulfur vacancies, and edges to the hydrogen evolution reaction catalytic activity of porous molybdenum disulfide nanosheets, J. Am. Chem. Soc. 138 (25) (2016) 7965–7972, https://doi.org/10.1021/jacs.6b03714.
[26] P. Liu, J. Zhu, J. Zhang, P. Xi, K. Tao, D. Gao, D. Xue, P dopants triggered new basal plane active sites and enlarged interlayer spacing in MoS_2 nanosheets toward electrocatalytic hydrogen evolution, ACS Energy Lett. 2 (4) (2017) 745–752, https://doi.org/10.1021/acsenergylett.7b00111.
[27] C. Tsai, H. Li, S. Park, J. Park, H.S. Han, J.K. Nørskov, X. Zheng, F. Abild-Pedersen, Electrochemical generation of sulfur vacancies in the basal plane of MoS_2 for hydrogen evolution, Nat. Commun. 8 (1) (2017) 15113, https://doi.org/10.1038/ncomms15113.
[28] M.A.R. Anjum, H.Y. Jeong, M.H. Lee, H.S. Shin, J.S. Lee, Efficient hydrogen evolution reaction catalysis in alkaline media by all-in-one MoS_2 with multifunctional active sites, Adv. Mater. 30 (20) (2018) 1707105, https://doi.org/10.1002/adma.201707105.
[29] X. Wang, Y. Zhang, H. Si, Q. Zhang, J. Wu, L. Gao, X. Wei, Y. Sun, Q. Liao, Z. Zhang, K. Ammarah, L. Gu, Z. Kang, Y. Zhang, Single-atom vacancy defect to trigger high-efficiency hydrogen evolution of MoS_2, J. Am. Chem. Soc. 142 (9) (2020) 4298–4308, https://doi.org/10.1021/jacs.9b12113.
[30] D. Kong, H. Wang, J.J. Cha, M. Pasta, K.J. Koski, J. Yao, Y. Cui, Synthesis of MoS_2 and $MoSe_2$ films with vertically aligned layers, Nano Lett. 13 (3) (2013) 1341–1347, https://doi.org/10.1021/nl400258t.
[31] J. Kibsgaard, Z. Chen, B.N. Reinecke, T.F. Jaramillo, Engineering the surface structure of MoS_2 to preferentially expose active edge sites for electrocatalysis, Nat. Mater. 11 (11) (2012) 963–969, https://doi.org/10.1038/nmat3439.
[32] Y. He, P. Tang, Z. Hu, Q. He, C. Zhu, L. Wang, Q. Zeng, P. Golani, G. Gao, W. Fu, Z. Huang, C. Gao, J. Xia, X. Wang, X. Wang, C. Zhu, Q.M. Ramasse, A. Zhang, B. An, Y. Zhang, S. Martí-Sánchez, J.R. Morante, L. Wang, B.K. Tay, B.I. Yakobson, A. Trampert, H. Zhang, M. Wu, Q.J. Wang, J. Arbiol, Z. Liu, Engineering grain boundaries at the 2D limit for the hydrogen evolution reaction, Nat. Commun. 11 (1) (2020) 57, https://doi.org/10.1038/s41467-019-13631-2.
[33] S. Li, S. Wang, M.M. Salamone, A.W. Robertson, S. Nayak, H. Kim, S.C.E. Tsang, M. Pasta, J.H. Warner, Edge-enriched 2D MoS_2 thin films grown by chemical vapor deposition for enhanced catalytic performance, ACS Catal. 7 (1) (2016) 877–886, https://doi.org/10.1021/acscatal.6b02663.
[34] H. Wang, X. Xiao, S. Liu, C.-L. Chiang, X. Kuai, C.-K. Peng, Y.-C. Lin, X. Meng, J. Zhao, J. Choi, Y.-G. Lin, J.-M. Lee, L. Gao, Structural and electronic optimization of MoS_2 edges for hydrogen evolution, J. Am. Chem. Soc. 141 (46) (2019) 18578–18584, https://doi.org/10.1021/jacs.9b09932.
[35] Z. Zhang, Y. Wang, X. Leng, V.H. Crespi, F. Kang, R. Lv, Controllable edge exposure of MoS_2 for efficient hydrogen evolution with high current density, ACS Appl. Energy Mater. 1 (3) (2018) 1268–1275, https://doi.org/10.1021/acsaem.8b00010.
[36] Q. Zhou, S. Su, P. Cheng, X. Hu, X. Gao, Z. Zhang, J.-M. Liu, Vertically conductive MoS_2 pyramids with a high density of active edge sites for efficient hydrogen evolution, J. Mater. Chem. C 8 (9) (2020) 3017–3022, https://doi.org/10.1039/c9tc05872a.
[37] J. Joyner, E.F. Oliveira, H. Yamaguchi, K. Kato, S. Vinod, D.S. Galvao, D. Salpekar, S. Roy, U. Martinez, C.S. Tiwary, S. Ozden, P.M. Ajayan, Graphene supported MoS_2 structures with high defect density for an efficient HER electrocatalysts, ACS Appl. Mater. Interfaces 12 (11) (2020) 12629–12638, https://doi.org/10.1021/acsami.9b17713.
[38] J. Benson, M. Li, S. Wang, P. Wang, P. Papakonstantinou, Electrocatalytic hydrogen evolution reaction on edges of a few layer molybdenum disulfide nanodots, ACS Appl. Mater. Interfaces 7 (25) (2015) 14113–14122, https://doi.org/10.1021/acsami.5b03399.
[39] Y. Li, K. Yin, L. Wang, X. Lu, Y. Zhang, Y. Liu, D. Yan, Y. Song, S. Luo, Engineering MoS_2 nanomesh with holes and lattice defects for highly active hydrogen evolution reaction, Appl. Catal. B, Environ. 239 (2018) 537–544, https://doi.org/10.1016/j.apcatb.2018.05.080.
[40] J. Zhu, Z.-C. Wang, H. Dai, Q. Wang, R. Yang, H. Yu, M. Liao, J. Zhang, W. Chen, Z. Wei, N. Li, L. Du, D. Shi, W. Wang, L. Zhang, Y. Jiang, G. Zhang, Boundary activated hydrogen evolution reaction on monolayer MoS_2, Nat. Commun. 10 (1) (2019) 1348, https://doi.org/10.1038/s41467-019-09269-9.
[41] L. Tao, X. Duan, C. Wang, X. Duan, S. Wang, Plasma-engineered MoS_2 thin-film as an efficient electrocatalyst for hydrogen evolution reaction, Chem. Commun. 51 (35) (2015) 7470–7473, https://doi.org/10.1039/c5cc01981h.
[42] C.-C. Cheng, A.-Y. Lu, C.-C. Tseng, X. Yang, M.N. Hedhili, M.-C. Chen, K.-H. Wei, L.-J. Li, Activating basal-plane catalytic activity of two-dimensional MoS_2 monolayer with remote hydrogen plasma, Nano Energy 30 (2016) 846–852, https://doi.org/10.1016/j.nanoen.2016.09.010.
[43] S. Li, S. Zhou, X. Wang, P. Tang, M. Pasta, J.H. Warner, Increasing the electrochemical activity of basal plane sites in porous 3D edge rich MoS_2 thin films for the hydrogen evolution reaction, Mater. Today Energy 13 (2019) 134–144, https://doi.org/10.1016/j.mtener.2019.05.002.
[44] G. Ye, Y. Gong, J. Lin, B. Li, Y. He, S.T. Pantelides, W. Zhou, R. Vajtai, P.M. Ajayan, Defects engineered monolayer MoS_2 for improved hydrogen evolution reaction, Nano Lett. 16 (2) (2016) 1097–1103, https://doi.org/10.1021/acs.nanolett.5b04331.
[45] C. Meng, M.-C. Lin, X.-W. Du, Y. Zhou, Molybdenum disulfide modified by laser irradiation for catalyzing hydrogen evolution, ACS Sustain. Chem. Eng. 7 (7) (2019) 6999–7003, https://doi.org/10.1021/acssuschemeng.8b06717.
[46] Z. Wang, Q. Li, H. Xu, C. Dahl-Petersen, Q. Yang, D. Cheng, D. Cao, F. Besenbacher, J.V. Lauritsen, S. Helveg, M. Dong, Controllable etching of MoS_2 basal planes for enhanced hydrogen evolution through the formation of active edge sites, Nano Energy 49 (2018) 634–643, https://doi.org/10.1016/j.nanoen.2018.04.067.
[47] P. Zhang, H. Xiang, L. Tao, H. Dong, Y. Zhou, T.S. Hu, X. Chen, S. Liu, S. Wang, S. Garaj, Chemically activated MoS_2 for efficient hydrogen production, Nano Energy 57 (2019) 535–541, https://doi.org/10.1016/j.nanoen.2018.12.045.
[48] L. Dong, S. Lin, L. Yang, J. Zhang, C. Yang, D. Yang, H. Lu, Spontaneous exfoliation and tailoring of MoS_2 in mixed solvents, Chem. Commun. 50 (100) (2014) 15936–15939, https://doi.org/10.1039/c4cc07238c.
[49] S. Su, Q. Zhou, Z. Zeng, D. Hu, X. Wang, M. Jin, X. Gao, R. Nötzel, G. Zhou, Z. Zhang, J. Liu, Ultrathin alumina mask-assisted nanopore patterning on monolayer MoS_2 for highly catalytic efficiency in hydrogen evolution reaction, ACS Appl. Mater. Interfaces 10 (9) (2018) 8026–8035, https://doi.org/10.1021/acsami.7b19197.
[50] L. Pei, H. Qiao, B. Chen, X. Zhu, R.A. Davis, K. Zhu, L. Xia, P. Dong, M. Ye, J. Shen, Pt edge-doped MoS_2: activating the active sites for maximized hydrogen evolution reaction performance, Small 17 (52) (2021) 2104245, https://doi.org/10.1002/smll.202104245.
[51] A. Bala, A. Sen, Y.-H. Kim, Y.-M. Kim, S. Gandla, H. Park, S. Kim, Large-area MoS_2 nanosheets with triangular nanopore arrays as active and robust electrocatalysts for hydrogen evolution, J. Phys. Chem. C 126 (23) (2022) 9696–9703, https://doi.org/10.1021/acs.jpcc.2c01859.
[52] J.M. Thomas, E.L. Evans, Enhanced reactivity at dislocations in layer structures, Nature 214 (5084) (1967) 167–168, https://doi.org/10.1038/214167a0.
[53] O.P. Bahl, E.L. Evans, J.M. Thomas, The identification and some properties of point defects and non-basal dislocations in molybdenite surfaces, Proc. R. Soc. Lond. Ser. A, Math. Phys. Sci. 306 (1484) (1968) 53–65, https://doi.org/10.1098/rspa.1968.0137.
[54] M.K. Agarwal, B. Joseph, Dislocation etching in molybdenite, J. Mater. Sci. 9 (8) (1974) 1262–1264, https://doi.org/10.1007/bf00551840.
[55] M.K. Agarwal, J.D. Kshatriya, P.D. Patel, P.K. Garg, Etching and dissolution kinetics of $MoSe_2$ single crystal, J. Mater. Sci. 17 (6) (1982) 1671–1674, https://doi.org/10.1007/bf00540794.
[56] W. Kautek, H. Gerischer, Anisotropic photocorrosion of n-type MoS_2, $MoSe_2$, and WSe_2 single crystal surfaces: the role of cleavage steps, line and screw dislocations, Surf. Sci. 119 (1) (1982) 46–60, https://doi.org/10.1016/0039-6028(82)90186-8.
[57] R. Tenne, A. Wold, Passivation of recombination centers in n-WSe_2 yields high efficiency (> 14%) photoelectrochemical cell, Appl. Phys. Lett. 47 (7) (1985) 707–709, https://doi.org/10.1063/1.96066.
[58] D. Mahalu, M. Peisach, W. Jaegermann, A. Wold, R. Tenne, Controlled photocorrosion of tungsten diselenide: influence of molecular oxygen, J. Phys. Chem. 94 (21) (1990) 8012–8013, https://doi.org/10.1021/j100384a005.
[59] R. Tenne, K. Eherman, D. Mahalu, M. Peisach, W. Kautek, A. Wold, R. Matson, D.H. Waldeck, The WSe_2/tungsten-oxide interface: structure and photoluminescence, Ber. Bunsenges. Phys. Chem. 97 (5) (1993) 702–708, https://doi.org/10.1002/bbpc.19930970510.
[60] B. Munkhbat, A.B. Yankovich, D.G. Baranov, R. Verre, E. Olsson, T.O. Shegai, Transition metal dichalcogenide metamaterials with atomic precision, Nat. Commun. 11 (1) (2020) 4604, https://doi.org/10.1038/s41467-020-18428-2.

[61] H. Park, J. Lee, G. Han, A. AlMutairi, Y.-H. Kim, J. Lee, Y.-M. Kim, Y.J. Kim, Y. Yoon, S. Kim, Nano-patterning on multilayer MoS_2 via block copolymer lithography for highly sensitive and responsive phototransistors, Commun. Mater. 2 (1) (2021) 94, https://doi.org/10.1038/s43246-021-00197-0.
[62] D.R. Danielsen, A. Lyksborg-Andersen, K.E.S. Nielsen, B.S. Jessen, T.J. Booth, M.-H. Doan, Y. Zhou, P. Bøggild, L. Gammelgaard, Super-resolution nanolithography of two-dimensional materials by anisotropic etching, ACS Appl. Mater. Interfaces 13 (35) (2021) 41886–41894, https://doi.org/10.1021/acsami.1c09923.
[63] X. Sang, X. Li, W. Zhao, J. Dong, C.M. Rouleau, D.B. Geohegan, F. Ding, K. Xiao, R.R. Unocic, In situ edge engineering in two-dimensional transition metal dichalcogenides, Nat. Commun. 9 (1) (2018) 2051, https://doi.org/10.1038/s41467-018-04435-x.
[64] M.G. Stanford, P.D. Rack, D. Jariwala, Emerging nanofabrication and quantum confinement techniques for 2D materials beyond graphene, npj 2D Mater. Appl. 2 (1) (2018) 20, https://doi.org/10.1038/s41699-018-0065-3.
[65] G. Li, D. Zhang, Y. Yu, S. Huang, W. Yang, L. Cao, Activating MoS_2 for pH-universal hydrogen evolution catalysis, J. Am. Chem. Soc. 139 (45) (2017) 16194–16200, https://doi.org/10.1021/jacs.7b07450.
[66] Y. Liu, J. Wu, K.P. Hackenberg, J. Zhang, Y.M. Wang, Y. Yang, K. Keyshar, J. Gu, T. Ogitsu, R. Vajtai, J. Lou, P.M. Ajayan, B.C. Wood, B.I. Yakobson, Self-optimizing, highly surface-active layered metal dichalcogenide catalysts for hydrogen evolution, Nat. Energy 2 (9) (2017) 17127, https://doi.org/10.1038/nenergy.2017.127.
[67] M. Ledendecker, J.S. Mondschein, O. Kasian, S. Geiger, D. Göhl, M. Schalenbach, A. Zeradjanin, S. Cherevko, R.E. Schaak, K. Mayrhofer, Stability and activity of non-noble-metal-based catalysts toward the hydrogen evolution reaction, Angew. Chem., Int. Ed. 56 (33) (2017) 9767–9771, https://doi.org/10.1002/anie.201704021.
[68] L. Li, Z. Qin, L. Ries, S. Hong, T. Michel, J. Yang, C. Salameh, M. Bechelany, P. Miele, D. Kaplan, M. Chhowalla, D. Voiry, Role of sulfur vacancies and undercoordinated Mo regions in MoS_2 nanosheets toward the evolution of hydrogen, ACS Nano 13 (6) (2019) 6824–6834, https://doi.org/10.1021/acsnano.9b01583.
[69] MoS_2 – molybdenum disulfide, https://www.hqgraphene.com/MoS2.php. (Accessed 29 November 2023).
[70] Z. Huang, P.D. Wolf, R. Poddar, C. Li, A. Mark, M.R. Nellist, Y. Chen, J. Jiang, G. Papastavrou, S.W. Boettcher, C. Xiang, B.S. Brunschwig, PeakForce scanning electrochemical microscopy with nanoelectrode probes, Microscopy Today 24 (6) (2016) 18–25, https://doi.org/10.1017/s1551929516000882.
[71] G. Wulff, XXV. Zur frage der geschwindigkeit des wachsthums und der auflösung der krystallflächen, Z. Kristallogr., Cryst. Mater. 34 (1–6) (1901) 449–530, https://doi.org/10.1524/zkri.1901.34.1.449.
[72] S. Wang, Y. Rong, Y. Fan, M. Pacios, H. Bhaskaran, K. He, J.H. Warner, Shape evolution of monolayer MoS_2 crystals grown by chemical vapor deposition, Chem. Mater. 26 (22) (2014) 6371–6379, https://doi.org/10.1021/cm5025662.
[73] M. Li, L. Li, Y. Fan, F. Jiao, D. Geng, W. Hu, From top to down – recent advances in etching of 2D materials, Adv. Mater. Interfaces 9 (31) (2022) 2201334, https://doi.org/10.1002/admi.202201334.
[74] Z. Huang, W. Deng, Z. Zhang, B. Zhao, H. Zhang, D. Wang, B. Li, M. Liu, Y. Huangfu, X. Duan, Terminal atom-controlled etching of 2D-TMDs, Adv. Mater. (2023) 2211252, https://doi.org/10.1002/adma.202211252.
[75] Y. Yang, H. He, H. Xian, J. Xi, X. Wu, A. Chen, J. Zhu, H. Xu, Periodic and non-periodic stacking in molybdenite (MoS_2) revealed by STEM, Am. Mineral. 107 (6) (2022) 997–1006, https://doi.org/10.2138/am-2022-8019.
[76] F.A. Cevallos, S. Guo, H. Heo, G. Scuri, Y. Zhou, J. Sung, T. Taniguchi, K. Watanabe, P. Kim, H. Park, R.J. Cava, Liquid salt transport growth of single crystals of the layered dichalcogenides MoS_2 and WS_2, Cryst. Growth Des. 19 (10) (2019) 5762–5767, https://doi.org/10.1021/acs.cgd.9b00785.
[77] L. Houben, A.N. Enyashin, Y. Feldman, R. Rosentsveig, D.G. Stroppa, M. Bar-Sadan, Diffraction from disordered stacking sequences in MoS_2 and WS_2 fullerenes and nanotubes, J. Phys. Chem. C 116 (45) (2012) 24350–24357, https://doi.org/10.1021/jp3080139.
[78] H. Park, M. Rahman, A. Bala, Y.-H. Kim, A. Sen, Y.-M. Kim, J. Lee, S. Kim, Nanoscale patterning on layered MoS_2 with stacking-dependent morphologies and optical tunning for phototransistor applications, Mater. Today Nano 23 (2023) 100367, https://doi.org/10.1016/j.mtnano.2023.100367.
[79] A. Dewambrechies, A.Y. Polyakov, B. Küçüköz, T.O. Shegai, Enhanced second-order nonlinearities at strained ultrasharp zigzag edges in multilayer MoS_2, J. Phys. Chem. C 127 (31) (2023) 15395–15405, https://doi.org/10.1021/acs.jpcc.3c03812.
[80] Y. Yu, S.-Y. Huang, Y. Li, S.N. Steinmann, W. Yang, L. Cao, Layer-dependent electrocatalysis of MoS_2 for hydrogen evolution, Nano Lett. 14 (2) (2014) 553–558, https://doi.org/10.1021/nl403620g.
[81] Y. He, Q. He, L. Wang, C. Zhu, P. Golani, A.D. Handoko, X. Yu, C. Gao, M. Ding, X. Wang, F. Liu, Q. Zeng, P. Yu, S. Guo, B.I. Yakobson, L. Wang, Z.W. Seh, Z. Zhang, M. Wu, Q.J. Wang, H. Zhang, Z. Liu, Self-gating in semiconductor electrocatalysis, Nat. Mater. 18 (10) (2019) 1098–1104, https://doi.org/10.1038/s41563-019-0426-0.
[82] A.W. Bott, Electrochemistry of semiconductors, Curr. Sep. 17 (1998) 87–91, http://www.currentseparations.com/issues/17-3/cs-17-3d.pdf.
[83] H. Lind, B. Wickman, J. Halim, G. Montserrat-Sisó, A. Hellman, J. Rosen, Hydrogen evolution reaction for vacancy-ordered i-MXenes and the impact of proton absorption into the vacancies, Adv. Sustain. Syst. 5 (2) (2020) 2000158, https://doi.org/10.1002/adsu.202000158.
[84] Y. Wang, J.C. Kim, R.J. Wu, J. Martinez, X. Song, J. Yang, F. Zhao, A. Mkhoyan, H.Y. Jeong, M. Chhowalla, Van der Waals contacts between three-dimensional metals and two-dimensional semiconductors, Nature 568 (7750) (2019) 70–74, https://doi.org/10.1038/s41586-019-1052-3.
[85] Y. Wang, J.C. Kim, Y. Li, K.Y. Ma, S. Hong, M. Kim, H.S. Shin, H.Y. Jeong, M. Chhowalla, P-type electrical contacts for 2D transition-metal dichalcogenides, Nature 610 (7930) (2022) 61–66, https://doi.org/10.1038/s41586-022-05134-w.
[86] M. Li, X. Bi, R. Wang, Y. Li, G. Jiang, L. Li, C. Zhong, Z. Chen, J. Lu, Relating catalysis between fuel cell and metal-air batteries, Matter 2 (1) (2020) 32–49, https://doi.org/10.1016/j.matt.2019.10.007.
[87] S. Jiao, Z. Yao, F. Xue, Y. Lu, M. Liu, H. Deng, X. Ma, Z. Liu, C. Ma, H. Huang, S. Ruan, Y.-J. Zeng, Defect-rich one-dimensional MoS_2 hierarchical architecture for efficient hydrogen evolution: coupling of multiple advantages into one catalyst, Appl. Catal. B, Environ. 258 (2019) 117964, https://doi.org/10.1016/j.apcatb.2019.117964.
[88] J. Yang, Y. Wang, M.J. Lagos, V. Manichev, R. Fullon, X. Song, D. Voiry, S. Chakraborty, W. Zhang, P.E. Batson, L. Feldman, T. Gustafsson, M. Chhowalla, Single atomic vacancy catalysis, ACS Nano 13 (9) (2019) 9958–9964, https://doi.org/10.1021/acsnano.9b05226.
[89] G.L. Frey, S. Elani, M. Homyonfer, Y. Feldman, R. Tenne, Optical-absorption spectra of inorganic fullerene-like MS_2 (M = Mo, W), Phys. Rev. B 57 (11) (1998) 6666–6671, https://doi.org/10.1103/physrevb.57.6666.
[90] A.Y. Polyakov, L. Yadgarov, R. Popovitz-Biro, V.A. Lebedev, I. Pinkas, R. Rosentsveig, Y. Feldman, A.E. Goldt, E.A. Goodilin, R. Tenne, Decoration of WS_2 nanotubes and fullerene-like MoS_2 with gold nanoparticles, J. Phys. Chem. C 118 (4) (2014) 2161–2169, https://doi.org/10.1021/jp407388h.
[91] A.Y. Polyakov, D.A. Kozlov, V.A. Lebedev, R.G. Chumakov, A.S. Frolov, L.V. Yashina, M.N. Rumyantseva, E.A. Goodilin, Gold decoration and photoresistive response to nitrogen dioxide of WS_2 nanotubes, Chemistry, Eur. J. 24 (71) (2018) 18952–18962, https://doi.org/10.1002/chem.201803502.
[92] A.Y. Polyakov, A.V. Nesterov, A.E. Goldt, V. Zubyuk, T. Dolgova, L. Yadgarov, B. Visic, A.A. Fedyanin, R. Tenne, E.A. Goodilin, Optical properties of multilayer films of nanocomposites based on WS_2 nanotubes decorated with gold nanoparticles, J. Phys. Conf. Ser. 643 (2015) 012046, https://doi.org/10.1088/1742-6596/643/1/012046.
[93] C.L. Bentley, M. Kang, F.M. Maddar, F. Li, M. Walker, J. Zhang, P.R. Unwin, Electrochemical maps and movies of the hydrogen evolution reaction on natural crystals of molybdenite (MoS_2): basal vs. edge plane activity, Chem. Sci. 8 (9) (2017) 6583–6593, https://doi.org/10.1039/c7sc02545a.
[94] C.L. Bentley, P.R. Unwin, Nanoscale electrochemical movies and synchronous topographical mapping of electrocatalytic materials, Faraday Discuss. 210 (2018) 365–379, https://doi.org/10.1039/c8fd00028j.
[95] B. Tao, P.R. Unwin, C.L. Bentley, Nanoscale variations in the electrocatalytic activity of layered transition-metal dichalcogenides, J. Phys. Chem. C 124 (1) (2019) 789–798, https://doi.org/10.1021/acs.jpcc.9b10279.
[96] L.E. Strange, J. Yadav, S. Garg, P.S. Shinde, J.W. Hill, C.M. Hill, P. Kung, S. Pan, Investigating the redox properties of two-dimensional MoS_2 using photoluminescence spectroelectrochemistry and scanning electrochemical cell microscopy, J. Phys. Chem. Lett. 11 (9) (2020) 3488–3494, https://doi.org/10.1021/acs.jpclett.0c00769.
[97] Y. Liu, C. Jin, Y. Liu, K.H. Ruiz, H. Ren, Y. Fan, H.S. White, Q. Chen, Visualization and quantification of electrochemical H_2 bubble nucleation at Pt, Au, and MoS_2 substrates, ACS Sens. 6 (2) (2020) 355–363, https://doi.org/10.1021/acssensors.0c00913.
[98] Y. Takahashi, Y. Kobayashi, Z. Wang, Y. Ito, M. Ota, H. Ida, A. Kumatani, K. Miyazawa, T. Fujita, H. Shiku, Y.E. Korchev, Y. Miyata, T. Fukuma, M. Chen, T. Matsue, High-resolution electrochemical mapping of the hydrogen evolution reaction on transition-metal dichalcogenide nanosheets, Angew. Chem., Int. Ed. 59 (9) (2020) 3601–3608, https://doi.org/10.1002/anie.201912863.
[99] C.L. Bentley, J. Edmondson, G.N. Meloni, D. Perry, V. Shkirskiy, P.R. Unwin, Nanoscale electrochemical mapping, Anal. Chem. 91 (1) (2018) 84–108, https://doi.org/10.1021/acs.analchem.8b05235.
[100] N.L. Ritzert, V.A. Szalai, T.P. Moffat, Mapping electron transfer at MoS_2 using scanning electrochemical microscopy, Langmuir 34 (46) (2018) 13864–13870, https://doi.org/10.1021/acs.langmuir.8b02731.
[101] H.-Y. Du, Y.-F. Huang, D. Wong, M.-F. Tseng, Y.-H. Lee, C.-H. Wang, C.-L. Lin, G. Hoffmann, K.-H. Chen, L.-C. Chen, Nanoscale redox mapping at the MoS_2-liquid interface, Nat. Commun. 12 (1) (2021) 1321, https://doi.org/10.1038/s41467-021-21660-z.
[102] T. Sun, H. Zhang, X. Wang, J. Liu, C. Xiao, S.U. Nanayakkara, J.L. Blackburn, M.V. Mirkin, E.M. Miller, Nanoscale mapping of hydrogen evolution on metallic and semiconducting MoS_2 nanosheets, Nanoscale Horiz. 4 (3) (2019) 619–624, https://doi.org/10.1039/c8nh00346g.
[103] H. Li, M. Du, M.J. Mleczko, A.L. Koh, Y. Nishi, E. Pop, A.J. Bard, X. Zheng, Kinetic study of hydrogen evolution reaction over strained MoS_2 with sulfur vacancies using scanning electrochemical microscopy, J. Am. Chem. Soc. 138 (15) (2016) 5123–5129, https://doi.org/10.1021/jacs.6b01377.

[104] C. Gu, T. Sun, Z. Wang, S. Jiang, Z. Wang, High resolution electrochemical imaging for sulfur vacancies on 2D molybdenum disulfide, Small Methods 7 (3) (2023) 2201529, https://doi.org/10.1002/smtd.202201529.

[105] S.A. Bacha, E. Farias, P. Garrigue, M. Zakhour, M. Nakhl, J.-L. Bobet, D. Zigah, Local enhancement of hydrogen production by the hydrolysis of $Mg_{17}Al_{12}$ with Mg "model" material, J. Alloys Compd. 895 (2) (2022) 162560, https://doi.org/10.1016/j.jallcom.2021.162560.